Spatio-temporal coordination at the maternal-fetal interface promotes trophoblast invasion and vascular remodeling in the first half of human pregnancy

Shirley Greenbaum[1,2,*,+], Inna Averbukh[1,+], Erin Soon[1,3,+], Gabrielle Rizzuto[4], Alex Baranski[1], Noah Greenwald[1,5], Marc Bosse[1], Eleni G. Jaswa[6], Zumana Khair[1], Shirley Kwok[1], Shiri Warshawsky[1], Geneva Miller[7], Morgan Schwartz[7], Will Graf[7], David Van Valen[7], Leeat Keren[8], Travis Hollmann[9], Matt van de Rijn[1], Michael Angelo[1, *]

[+]Equal contribution

[*]Correspondence: greenbaumsh@gmail.com (S.G.), mangelo0@stanford.edu (M.A.)

[1]Department of Pathology, Stanford University

[2]Department of Obstetrics & Gynecology, Hadassah-Hebrew University Medical Center

[3]Immunology Program, Stanford University

[4]Department of Pathology, UCSF

[5]Cancer Biology Program, Stanford University

[6]Department of Obstetrics, Gynecology & Reproductive Sciences, UCSF

[7]Division of Biology and Bioengineering, California Institute of Technology

[8]Department of Molecular Cell Biology, Weizmann Institute of Science

[9]Department of Pathology, Memorial Sloan Kettering Cancer Center

Abstract

Beginning in the first trimester, fetally derived extravillous trophoblasts (EVTs) invade the uterus and remodel its spiral arteries, transforming them into large, dilated blood vessels that lack smooth muscle and are partially lined with EVTs instead of vascular endothelium. Several mechanisms have been proposed to explain how EVTs coordinate with decidual cells to promote a tissue microenvironment conducive to spiral artery remodeling (SAR). However, it remains a matter of debate which immune and stromal cell types participate in these interactions, how this process evolves with respect to gestational age, and which anatomic routes are the predominate path of EVT invasion in humans. To elucidate this complex interplay, we used multiplexed ion beam imaging by time of flight with a 37-plex antibody panel to build the first spatio-temporal atlas of the human maternal-fetal interface in the first half of pregnancy at single-cell resolution. We analyzed ~500,000 cells and 588 spiral arteries within intact decidua from 66 patients between 6-20 weeks of gestation. Using custom machine learning algorithms for cell segmentation and classification, we evaluated the spatial distributions and phenotype of 20 maternal and five EVT populations with respect to gestational age and SAR. Gestational age substantially influenced the frequency of most maternal immune and stromal cells, with tolerogenic subsets expressing CD206, CD163, TIM-3, Galectin-9, and IDO-1 preferentially enriched at later time points. In contrast, SAR progression, and not gestational age, preferentially correlated with local invasion of EVTs. Lastly, by comparing spatial co-occurrence and phenotype of decidual interstitial, perivascular and intravascular EVTs with respect to SAR progression, we developed a statistical model suggesting an intravasation mechanism as the predominant route of EVT invasion in superficial decidua. Taken together, these results support a coordinated model of decidualization in which increasing gestational age drives a transition in maternal decidua towards a tolerogenic niche conducive to locally regulated, EVT-dependent SAR.

Introduction

The maternal-fetal interface is established when the trophoectoderm cells of the blastocyst invade the decidualizing endometrial stroma, ultimately forming the placenta. From that point forward, normal development depends on a complex interplay between maternal cells and placental trophoblasts that ultimately transforms the nascent womb into a specialized niche capable of meeting the metabolic demands of a growing hemi-allogeneic fetus while maintaining maternal tolerance[1–5]. Rather than being a single monotonic trend, this process is multifaceted and dynamic with respect to both tissue structure and gestational age (GA). Subsequent to implantation, decidual cellular composition shifts to one that is enriched for invasive extravillous trophoblasts (EVTs)[6]. During this transition, maternal and fetal cells remodel uterine spiral arteries into highly dilated vessels with minimal smooth muscle where EVTs have partially replaced the

maternal endothelium within the arterial lumen[7–9]. Spiral artery remodeling (SAR) in healthy pregnancies results in low-resistance vessels that can deliver blood to the intervillous space at low flow velocities that prevent damage to the placental architecture[10,11]. Conversely, impaired SAR, fewer tolerogenic maternal cells, and abnormal decidual invasion of EVTs have each been implicated in placenta-related obstetric complications, including preeclampsia, intrauterine growth restriction, and preterm birth[12,13]. Therefore, detailed investigation of the cell population dynamics at the maternal-fetal interface is key to understanding the biology of normal pregnancy and the pathophysiology of placenta-related obstetric complications.

Due to the poor feasibility of controlled studies in pregnant humans, much of what is known about maternal-fetal tolerance and SAR is based on pregnancy in small mammals[14]. Although some similarities exist, key facets of hemochorial placentation in humans are primate-specific, and in some cases are restricted even further to great apes[15–17]. For example, EVTs in mice only invade the superficial decidua, do not replace the vascular endothelium, and are thought to play a minor role in SAR compared to maternal uterine natural killer (NK) cells[18]. In contrast, EVTs in humans invade completely through the decidua into the inner third of the myometrium and are considered to be vital for adequate SAR[3,19,20]. Since the most extensive EVT invasion has been observed in humans, it may be a key adaptation that permitted upright, bipedal locomotion while maintaining adequate blood flow in the third trimester when development of the large fetal brain accounts for 60% of metabolic needs [21,22].

The study of human decidual remodeling is further complicated by additional inherent challenges. First, cell composition and structure are temporally dynamic; aggregating data across different GAs or observing a single time point may be misleading. As endometrial stromal cells shift towards a decidualized phenotype[23,24], the functions of maternal NK cells, T cells, and macrophages change dynamically in the first and second trimesters to promote a permissive niche conducive to villus attachment and invasion. This process necessarily establishes a gradient of EVT invasion that advances inward from the superficial decidua. Consequently, decidual structure and composition in focal regions can differ significantly from its bulk attributes. A second major challenge arises in understanding how these global dynamics are coupled to processes requiring spatial

92 coordination, such as those between maternal and placental cells in the local tissue
93 microenvironment. For example, periarterial decidual NK cells are thought to contribute
94 to SAR both by initiating smooth muscle breakdown and by secreting chemokines that
95 attract invading EVTs, while phagocytic macrophages are thought to facilitate clearance
96 of the resultant apoptotic debris[25–27]. Overall, formation of the human maternal-fetal
97 interface involves sophisticated spatiotemporal coordination such that tissue composition,
98 structure, and function are inextricably coupled. Unraveling this interdependence requires
99 an approach that can ascertain how these facets change over time in intact human tissue.

100 With this in mind, we constructed the first high dimensional spatio-temporal atlas
101 of the human maternal-fetal interface. We leveraged archival tissue banks to assemble a
102 cohort of maternal decidua from 66 women who underwent elective terminations of
103 otherwise healthy pregnancies at 6-20 weeks gestation. We then performed high
104 dimensional, subcellular imaging with multiplexed ion beam imaging by time of flight
105 (MIBI-TOF) [28] using a 37-plex antibody panel designed to comprehensively identify the
106 location, lineage, and function of all major maternal and placental cells. To understand
107 how SAR relates to local decidual composition, we developed new algorithms for
108 quantifying vascular morphology that enabled us to assign a remodeling score to each
109 individual artery. Comparison of these scores for 588 arteries revealed that the extent of
110 SAR to varies significantly with respect to GA. We then leveraged these discordances to
111 discern which changes in decidual composition and structure were preferentially driven
112 by GA, SAR, or both. Overall, the frequencies and relative proportions of maternal
113 immune cells exhibited a robust temporal dependence that permitted us to predict GA
114 based on these features alone. In contrast, we found that EVT invasion and perivascular
115 localization were the dominant drivers of SAR in the tissue microenvironment. Given
116 these findings, we then used our atlas to compare two models for the path of EVT
117 migration from the cytotrophoblast cell columns to maternal spiral arteries that have been
118 proposed previously: (1) intravasation, where EVTs first invade the decidua and then
119 enter arteries by traversing the arterial wall, and (2) extravasation, where EVTs enter
120 arteries directly at the basal plate[9]. Using statistical analyses correlating EVT phenotype
121 and location with the extent of arterial smooth muscle and endothelial loss, we found that
122 our spatiotemporal atlas was most consistent with an intravasation model. Taken

123 together, these investigations support a cooperative interplay in the first half of pregnancy
124 in which temporally dependent changes in decidual function permit placental EVTs to
125 extensively alter the maternal uterine vasculature.

126 Results

127 Multiplexed imaging of human decidua reveals the tolerogenic composition of the 128 maternal-fetal interface

129 As part of the Human BioMolecular Atlas Program (HuBMAP) initiative, we created
130 the first spatio-temporal tissue atlas of the human maternal-fetal interface in the first 20
131 weeks of pregnancy (Fig. 1a). The goal of this study was to comprehensively define the
132 structure and composition of decidua and to understand how it changes during the first
133 two trimesters with respect to two axes: GA and maternal SAR. To examine these issues,
134 we assembled a retrospective cohort of archival formalin-fixed, paraffin-embedded
135 placenta and decidua tissue from 74 patients who underwent elective termination of
136 pregnancies with no known fetal abnormalities. Archival tissue blocks were manually
137 screened by a perinatal pathologist in hematoxylin and eosin (H&E) stained tissue
138 sections to determine which samples contained decidua. Then, regions of decidua that
139 contained spiral arteries were demarcated, cored, and assembled into two tissue
140 microarrays (TMAs) of 1mm and 1.5 mm cores. The final dataset included samples for 6-
141 20 weeks of gestation (13.72±4.8 weeks) from 66 patients of varying parity (1.45±1.72),
142 age (28.17±5.9 years), body mass index (28.19±7.3 kg/m^2), and ethnicity (Fig. 1b-f,
143 Supplementary Table 1). Due to inherent limitations in how the tissue was procured,
144 precise anatomic locations could not be determined. However, 61 out 66 tissue blocks
145 contained placental villi, suggesting that the vast majority of this cohort was sampled from
146 decidua basalis (Supplementary Table 2, See methods).

147 Previous studies of intact tissue examining only one or a few cell populations at a
148 time reported shifts in maternal immune cells towards tolerogenic states that are
149 permissive to invasion by fetally derived EVTs[19]. To gain a more complete picture of the
150 complex cell-cell interactions that establish maternal tolerance in the first half of
151 pregnancy, we designed and validated a 37-plex antibody panel for simultaneously

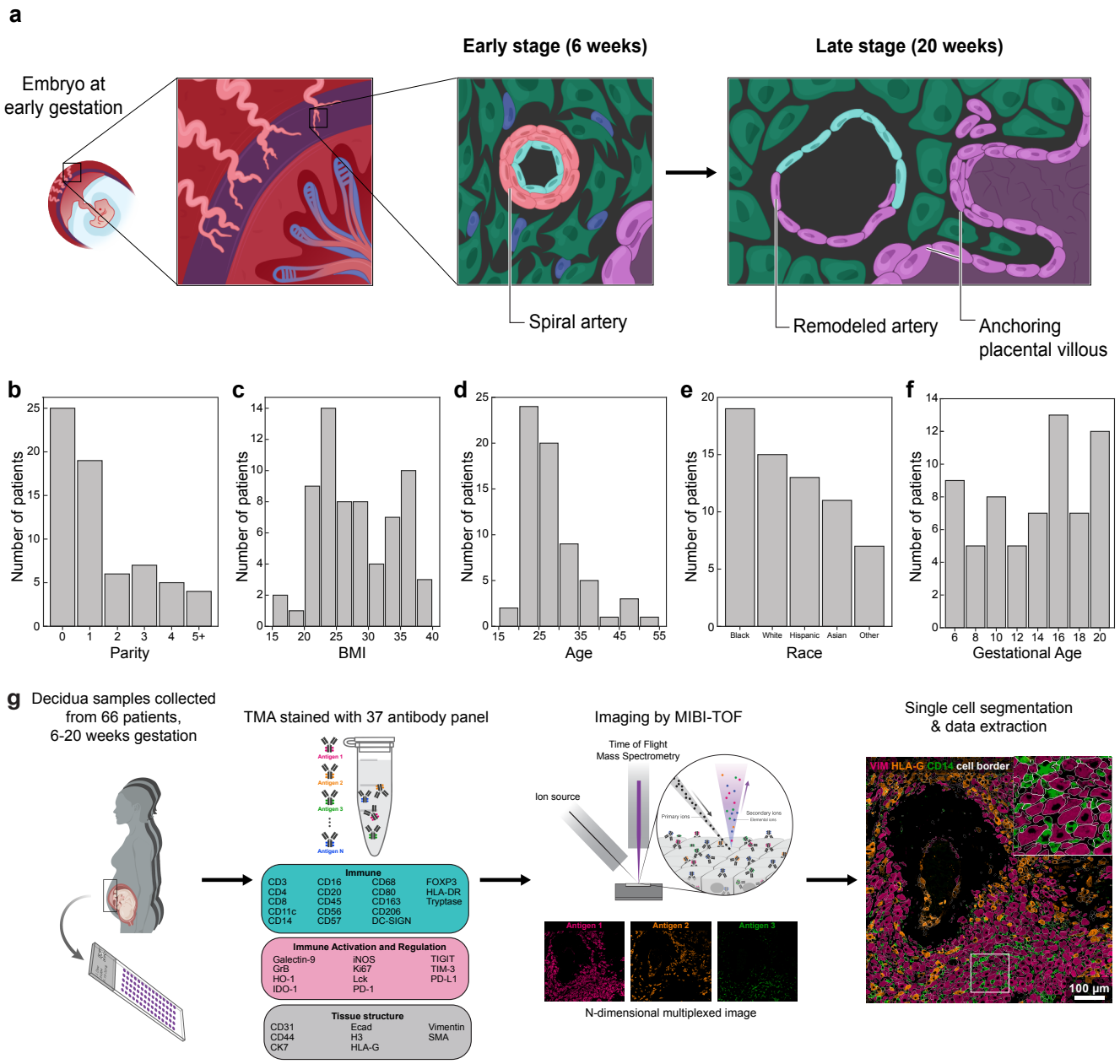

Figure 1 | Study design and workflow. a. Diagram of a human embryo in utero at 6 weeks gestation. First inset: the maternal-fetal interface consisting of decidua basalis (purple) with maternal spiral arteries (light pink) and fetal chorionic villi in the intervillous space (bottom right corner). Second inset: early stage (6 weeks) unremodeled spiral artery and progression to late stage (20 weeks) remodeled artery and anchoring fetal villi. **b.** Cohort parity distribution. **c.** Cohort distribution of body mass index (BMI). **d.** Cohort age distribution. **e.** Cohort ethnicity distribution. **f.** Cohort distribution of gestational age (GA). **g.** TMA construction, antibody panel, MIBI workflow, and single-cell segmentation.

mapping the functional state and location of all major maternal and fetal cell populations (Fig. 1g, See methods, Extended Data Fig. S1). In addition to canonical lineage defining

154 markers for fetal cells, maternal immune cells, fibroblasts, smooth muscle, endothelium,
155 and epithelium, we also quantified 10 functional markers previously implicated in maternal
156 immune tolerance, including TIM-3, Galectin-9, PD-1, PDL-1, and IDO-1 (Fig. 1g,
157 Extended Data Fig. S1)[29–34] . TMA sections were stained simultaneously with this
158 antibody panel and subsequently imaged at 500 nm resolution using MIBI-TOF (Fig. 1g).

159 Multiplexed images were denoised with a low-level image analysis pipeline as
160 described previously (Fig. 1g)[35]. To accurately capture the unique diversity of
161 morphologically distinct maternal and fetal cells, we used our previously validated custom
162 whole cell convolutional neural network, Mesmer[36] (See methods, Extended Data Fig.
163 S2a). We optimized this neural network for decidua-specific segmentation by training with
164 93,000 manually annotated single cell events from 25 decidual images, 15 of them from
165 our cohort. Applying this segmentation algorithm to our cohort images yielded 495,349
166 segmented cells in total, identified across 211 images (800μmx800μm, 2347±783 cells
167 per image). FlowSOM clustering[37] was used to assign 92% of whole cell segmented
168 events to 25 cell populations (Fig. 2a, b, See methods, Extended Data Fig. S2b, c,
169 Supplementary Table 3). These data (Fig. 2c-g) were then combined with whole-cell
170 segmentation masks to generate cell phenotype maps (CPM) in which each cell is colored
171 categorically by its respective population (Fig. 2h, Extended Data Fig. S2d). We then
172 determined whether cells expressed the functional markers by applying statistically
173 derived per-marker binary expression thresholds (see Methods, Extended Data Fig. S2e,
174 Supplementary Table 4). Noteworthy histological features—such as arteries, vessels,
175 glands, the cell columns, and decidual tissue boundaries were manually annotated in
176 collaboration with a perinatal pathologist.

177 Non-immune maternal (structural) cells accounted for the majority (56.3%) of all
178 segmented events in the decidua and were predominantly composed of decidual
179 fibroblasts (60.5%) and myofibroblasts (24.8%) with smaller contributions from vascular
180 endothelium (7.6%) and glandular epithelial cells (7.1%, Fig. 2b, c). Maternal immune
181 cells (31% of all cells) were dominated by macrophages (47.6% of immune) and NK cells
182 (42.6% of immune) with minor contributions from T (8% of immune), dendritic (1.3% of
183 immune), and mast cells (0.5% of immune). We identified a total of five decidual

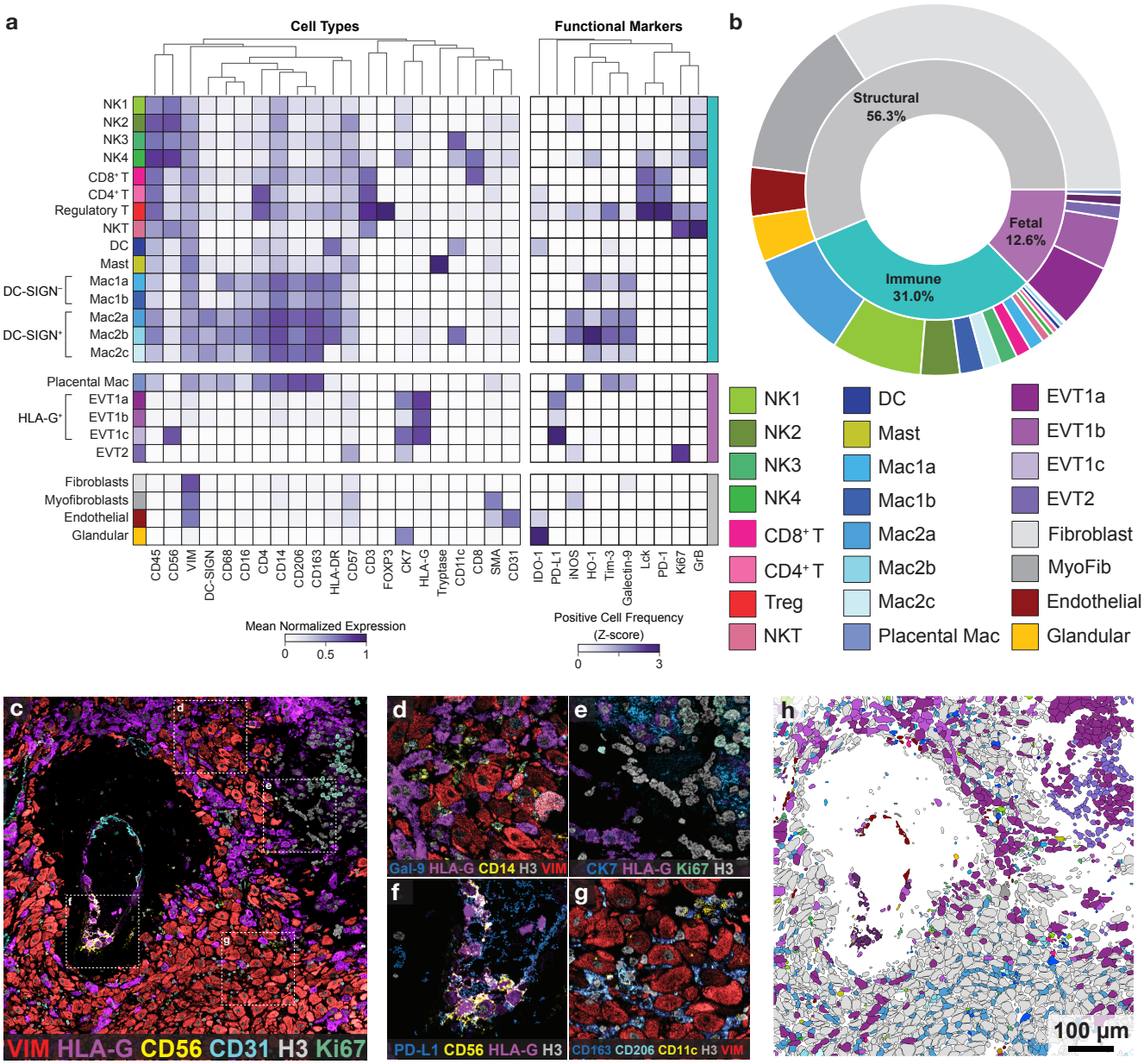

Figure 2 | Multiplexed imaging of human decidua reveals the immune tolerance-conducive composition of the maternal fetal interface. a. Cell lineage assignments showing mean normalized expression of lineage markers (left) and functional marker positive cell frequency (right, Z-score). Columns (markers) are hierarchically clustered. **b.** Cell lineage abundances across our cohort. Placental mac: Placental macrophage; MyoFib: Myofibroblast. **c.** Representative MIBI field of view color overlay of a 20 week sample. Red = VIM, vimentin, purple = HLA-G, yellow = CD56, cyan = CD31, grey = H3, green = Ki67. **d.** Inset of **c**, interstitial fetal EVTs. Blue = Galectin-9, purple = HLA-G, yellow = CD14, grey = H3, red = VIM **e.** Inset of **c**, showing anchoring villous cell column to decidua interface. Blue = CK7, cytokeratin7, purple = HLA-G, green = Ki67, grey = H3. **f.** Inset of **c**, showing intravascular EVTs. Blue = PD-L1, purple = HLA-G, yellow = CD56, grey = H3. **g.** Inset of **c**, showing decidual stromal cells (fibroblasts) and macrophages. Blue = CD163, cyan = CD206, yellow = CD11c, grey = H3, red = vimentin. **h.** Cell lineage assignments overlaid onto the cell-segmentation output to produce a cell phenotype map.

184 macrophage ($CD14^+$) populations, ubiquitously co-expressing CD163 and CD206,
185 consistent with an M2-polarized, tolerogenic phenotype[38] (Fig. 2g). In line with previous
186 work showing pregnancy-specific recruitment, 77% of macrophages expressed DC-
187 SIGN[39] (Fig. 2a). We further classified DC-SIGN$^+$ macrophages into three subsets
188 (Mac2a, 2b, 2c) based on expression of CD11c (Mac2b, 2.7% of macrophages) or
189 absence of HLA-DR (Mac2c, 10.3% of macrophages). The majority (64%) of
190 macrophages were CD11c$^-$HLA-DR$^+$ (Mac2a). Macrophages lacking DC-SIGN (23% of
191 macrophages) were further categorized based on CD68 expression (CD68$^-$ Mac1b and
192 CD68$^+$ Mac1a) (Fig. 2a, b).

193 Four subsets of NK cells (CD3$^-$CD56$^+$) were identified based on combinatorial co-
194 expression of CD57, CD11c, and CD8. NK1 (CD57$^-$CD16^{low}) were the largest NK cell
195 population present, making up 59.7% of NK cells (Fig. 2a, b). The remaining three subsets
196 could be distinguished based on expression of CD57 (NK2, 25.8% of NK cells), CD11c
197 (NK3, 11.3% of NK cells), or CD8 (NK4, 3.2% of NK cells) (Fig. 2a, b). T cells consisted
198 of CD8$^+$ (53.2% of T cells), CD56$^+$ NKTs (28.8% of T cells), CD4$^+$ (17.1% of T cells), and
199 sparse numbers of regulatory T (Treg) cells (CD4$^+$FOXP3$^+$, 0.7% of T cells); while no B
200 cells were observed (Fig. 2a, b). Fetal cells (12.6% of all cells) primarily comprised four
201 subsets of EVTs that were delineated based on combinatorial expression of HLA-G, CK7,
202 CD57, and CD56 (Fig. 2a). HLA-G$^+$ interstitial EVT populations were CK7$^+$ (EVT1a,
203 44.6% of fetal cells), CK7$^-$ (EVT1b, 35.3% of fetal cells), or CD56$^+$ (EVT1c, 6.9% of fetal
204 cells) (Fig. 2c-f). EVT2 lacked HLA-G and were CD57$^-$CK7^{low} (EVT2, 9.4% of fetal cells).
205 Notably, placental macrophages (Hofbauer cells) located in chorionic villi constituted the
206 remainder (4.1%) of fetal cells and exhibited a cellular phenotype similar to that of Mac2c
207 (DC-SIGN$^+$HLA-DR$^-$) decidual macrophages (Fig. 2a).

208 As previously reported, we detected IDO-1 expression in glandular cells[29], but also
209 in vascular endothelium, where it has been previously reported to be scarce (12.3% of
210 endothelial cells were IDO-1$^+$, Fig. 2a)[34]. Our analysis revealed numerous functional
211 subsets of maternal cells, including TIM-3$^+$Galectin-9$^+$, iNOS$^+$, and HO-1$^+$ subsets of DC-
212 SIGN$^+$ macrophages, Galectin-9$^+$ fibroblasts (36.7% Galectin-9$^+$, Fig. 2d), and an
213 intriguing TIM-3$^+$Lck$^+$ subset of Tregs that accounted for >50% of this population (Fig. 2a,
214 b). Interestingly, both Tregs and NKT cells were highly proliferative (13.7% Ki67$^+$ Tregs,

215 17% Ki67$^+$ NKT cells), and with the notable exception of CD8$^+$ NK cells (22.9% GrB$^+$),
216 had higher frequencies of GrB (Granzyme B) expressing cells than any NK cell subset
217 (33.7% GrB$^+$ NKT, 19.5% GrB$^+$ Treg). Our highly multiplexed imaging platform confirmed
218 prior findings[32,39–41] and enabled us to enumerate an ensemble of functional states across
219 multiple lineages that were collectively consistent with maintaining a tolerogenic niche.

220 SAR progression is tightly correlated with the local tissue microenvironment

221 Perfusion of the intervillous space by uterine spiral arteries is the sole source of
222 oxygen and nutrients to the growing fetus after the establishment of arterial flow. During
223 the first half of pregnancy, these vessels undergo an extensive remodeling process that
224 culminates in dilated, non-contractile vessels depleted of smooth muscle and where the
225 maternal endothelium has been replaced by EVTs. While abnormal SAR is associated
226 with obstetric complications, such as intrauterine growth restriction and preeclampsia[12,13],
227 it is still not fully understood which cell populations directly participate in SAR, how this
228 process is locally regulated, and to what extent these changes are synchronized with GA.

229 We therefore used our spatiotemporal atlas of decidua to construct a SAR
230 trajectory to reveal how this process relates to temporal changes in decidua cell
231 composition and structure. Using artery size, smooth muscle layer disruption and loss,
232 endothelial continuity, EVT infiltration, and EVT endothelization to determine the extent
233 of SAR, we manually assigned each artery to one of five sequential remodeling stages
234 based on previously published criteria[42] (Fig. 3a). To ensure scoring was not biased by
235 patient demographics, the score of neighboring arteries, or the composition of nearby
236 stroma, scoring was performed on cropped images of each artery independently by
237 blinded experts. Out of 588 arteries, 186 were unremodeled and assigned to Stage 1 (Fig.
238 3b, c). Stage 2 arteries (300 arteries) were characterized by moderate smooth muscle
239 disruption and endothelial swelling (Fig. 3d, e). Stage 3 arteries (43 arteries) exhibited
240 more dilation, smooth muscle loss, and early endothelial disruption (Fig. 3f, g).
241 Progression to Stage 4 (34 arteries) was marked by the presence of EVTs within the
242 arterial lumen (Fig. 3h,i), while fully remodeled Stage 5 arteries (25 arteries) were
243 identified based on their very large size, near-complete smooth muscle loss, and EVT
244 endothelization (Fig. 3j, k, see Methods, Extended Data Fig. S3a, Supplementary Table

5).

Although SAR correlated with GA to some extent (Spearman's ρ=0.28, p-value = $1.5*10^{-12}$), in many cases artery staging and GA were discordant. For example, at least one late-stage artery (Stage 4-5) was present in 40% of week 8 samples, while minimally remodeled arteries were present throughout (Fig. 3l). Moreover, SAR staging of arteries from the same patient often varied significantly between tissue cores (32% of patients had arteries that differed by at least two stages), suggesting that this discordance could be highlighting aspects of SAR that are locally regulated by the tissue microenvironment (Fig. 3l, Extended Data Fig. S3b).

This decoupling of SAR and GA permitted us to identify changes in decidual composition that were predominantly driven by one or the other. We first developed a quantitative staging scheme for assigning a continuous, quantitative, and accurate remodeling score in an automated fashion. For each artery, we extracted 35 parameters describing the same aspects of arterial morphology that were used for manual scoring (Fig. 3m, see Methods, Extended Data Fig. S3d). Together with manual staging, we used this quantitative morphologic profile to construct a highly resolved pseudotime trajectory of SAR using linear discriminant analysis (LDA)[43] (Fig. 3m, n). We generated this trajectory by combining the 35 morphological features with our manually defined stage labels and applying LDA to project each artery with respect to a two-dimensional LDA space in which separation of arteries by their manually assigned stages is optimal (see Methods). This separation was mainly driven by artery shape and size, properties of the smooth muscle layer and EVT presence (see Methods, Supplementary Table 6).

We then defined a remodeling trajectory as the polynomial fit to artery points in this space and subsequently mapped each artery (a_i) to the nearest point along this curve (b_i, Fig. 3n inset, see Methods). Finally, a remodeling score (δ) was determined by calculating the distance along this curve from the point of origin (x_o) to b_i for each artery (See integral in Fig. 3n, Extended Data Fig. S3e, f, Supplementary Table 5). With our continuous remodeling score δ, we next defined a simple scheme to differentiate GA- and SAR-driven trends by performing linear regressions of cell frequency per image both as a function of GA and as a function of δ. Regression R^2 and p-values were used as proxies for trend

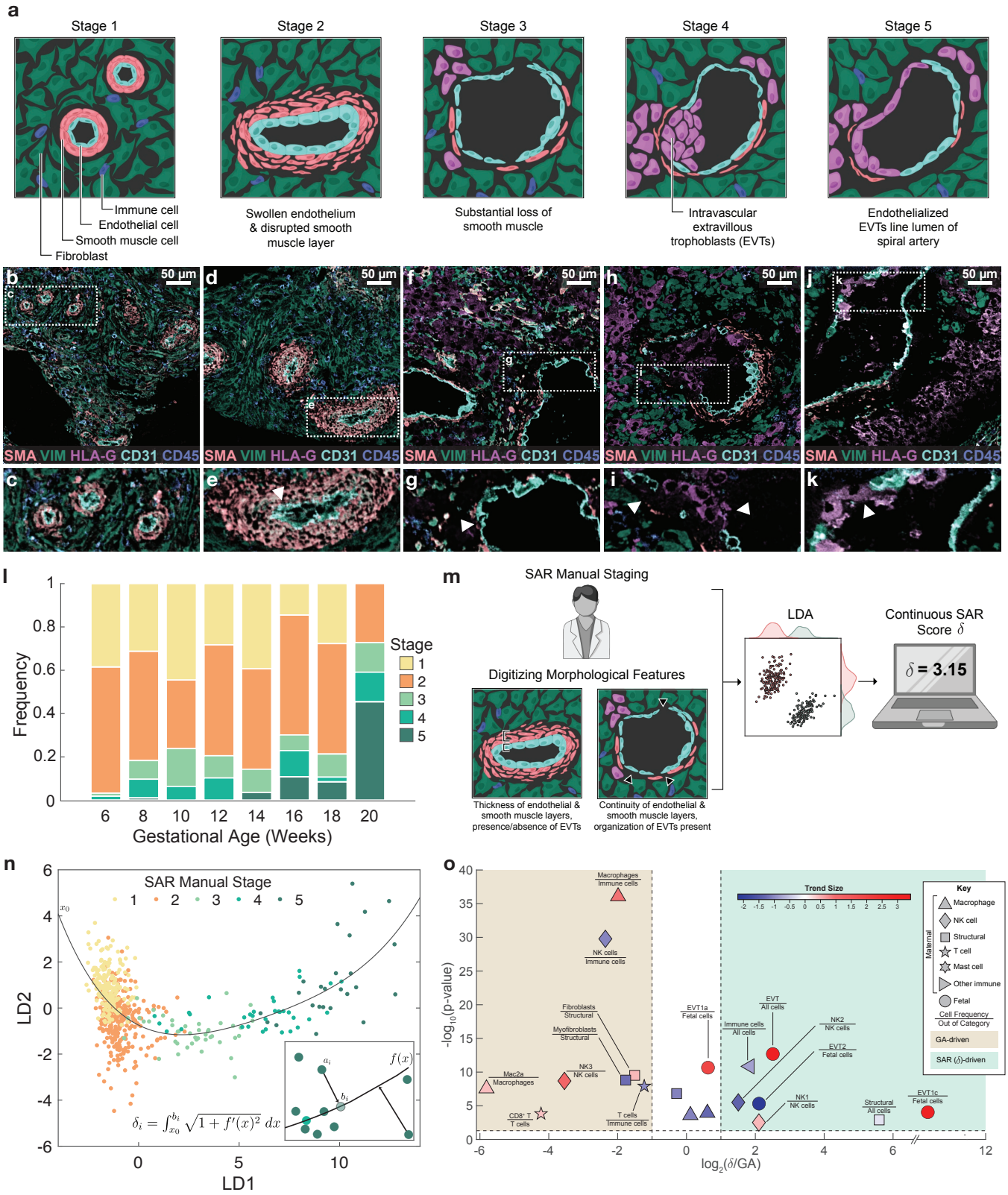
a
Stage 1
Stage 2
Stage 3
Stage 4
Stage 5
Immune cell
Endothelial cell
Smooth muscle cell
Fibroblast
Swollen endothelium & disrupted smooth muscle layer
Substantial loss of smooth muscle
Intravascular extravillous trophoblasts (EVTs)
Endothelialized EVTs line lumen of spiral artery
50 µm
SMA VIM HLA-G CD31 CD45
l
Frequency
Gestational Age (Weeks)
Stage
m
SAR Manual Staging
Digitizing Morphological Features
Thickness of endothelial & smooth muscle layers, presence/absence of EVTs
Continuity of endothelial & smooth muscle layers, organization of EVTs present
LDA
Continuous SAR Score δ
δ = 3.15
n
SAR Manual Stage
LD2
LD1
$\delta_i = \int_{x_0}^{b_i} \sqrt{1 + f'(x)^2}\, dx$
o
Trend Size
Key
Macrophage
NK cell
Structural
T cell
Mast cell
Other immune
Fetal
Maternal
Cell Frequency Out of Category
GA-driven
SAR (δ)-driven
-log10(p-value)
log2(δ/GA)

Figure 3 | Spiral Artery Remodeling (SAR) progression significantly influences maternal-fetal interface composition. a. Diagram showing key characteristics of SAR Stages 1-5, assessed manually. **b.** Representative MIBI color overlay of SAR manual Stage 1 arteries. VIM, vimentin; SMA, smooth muscle actin. **c.** Inset of **b**, showing SAR manual Stage 1 arteries. **d.** Representative MIBI color overlay of SAR manual Stage 2 arteries. **e.** Inset of **d**, showing one SAR manual Stage 2 artery. Arrowhead; swollen endothelial cells. **f.** Representative MIBI color overlay of SAR manual Stage 3 arteries. **g.** Inset of **f**, showing one SAR manual Stage 3 artery. Arrowhead; substantial loss of smooth muscle **h.** Representative MIBI color overlay of one SAR manual Stage 4 artery. **i.** Inset of **h**, showing one SAR manual Stage 4 artery. Arrowheads; intravascular EVTs. **j.** Representative MIBI color overlay of one SAR manual Stage 5 artery. **k.** Inset of **j**, showing one SAR manual Stage 5 artery. Arrowhead; endothelialized intravascular EVTs lining the spiral artery lumen. **l.** Distribution of SAR manual stages by gestational age (GA). **m.** Schematic of calculating the continuous SAR remodeling score (δ). Manual stages along with quantified digitized morphological features were used to construct a trajectory of SAR using LDA from which the continuous SAR score δ was calculated. **n.** Scatter of arteries in LDA space color coded by manually assigned stage. The polynomial fit depicts the remodeling trajectory. Inset: matching each artery point a_i to the SAR trajectory by finding the nearest point along trajectory b_i. The continuous SAR score δ was then defined as the distance from origin x_0 to b_i along the trajectory curve. **o.** Volcano plot distinguishing GA-driven from SAR (δ)-driven cell-type frequencies. X axis: $\log_2$ ratio of R^2 derived from linear regression against SAR (δ) and GA. Y axis: $-\log_{10}$ of the p-value for the better-fitting regression model. Points are color coded by the trend size observed in the better-fitting regression model.

quality and to assess significance, respectively. Trends where R^2 for GA and SAR differed by at least two-fold were classified as being driven predominately by a single process, while ones falling below this cutoff were classified as synchronized (Fig. 3o, see Methods, Extended Data Fig. S3g, h, Supplementary Table 7).

Consistent with previous studies reporting fewer interstitial EVTs in pregnancy complications that were related to impaired SAR, EVT decidual presence was better correlated with SAR than with GA (Log_2 R^2 ratio(δ:GA) = 2.5, p-value for δ =$1e^{-13}$). This increase in decidual EVTs with SAR was accompanied by a decrease in immune and structural cell frequencies (Fig. 3o). Within the EVT compartment, the frequency of EVT1c out of fetal cells exhibited the greatest bias for SAR (Log_2 R^2 ratio(δ:GA) = 10.3, p-value for δ = $9e^{-4}$, increase of 2.8 times the mean value, Fig. 3o), further highlighting this dependence. Changes in the relative proportion of cell types within the immune compartment were mostly driven by GA (Fig. 3o). Notably, the DC-SIGN$^+$ Mac2a subset which was previously reported to be pregnancy-specific[39] was heavily GA-biased (Log_2 R^2 ratio(δ:GA) = -5.8, p-value for GA = $3e^{-8}$, Fig. 3o), suggesting that this population is recruited in a manner that is agnostic to SAR. In contrast, the trade-offs within the NK cell compartment where the relative proportion of NK2 (CD57$^+$) diminished as NK1 (CD57$^-$) increased were SAR-dependent (Log_2 R^2 ratio(δ:GA) ≥ 1.5, p-value for δ ≤ 0.003, Fig.

3o). Interestingly, CD57 expression in human NKs results in a highly cytotoxic phenotype and has been shown to play a pivotal role in cancer immunosurveillance[44]. These trends suggest that during pregnancy, the reduction in cytotoxic mature NKs promotes a permissive niche where EVTs can invade and initiate SAR.

A lymphoid to myeloid shift in immune compartment composition is tightly correlated with GA

Our analyses indicated a robust, GA dependent shift from a lymphoid to myeloid dominated immune landscape, characterized by fewer NK and T cells and a concomitant

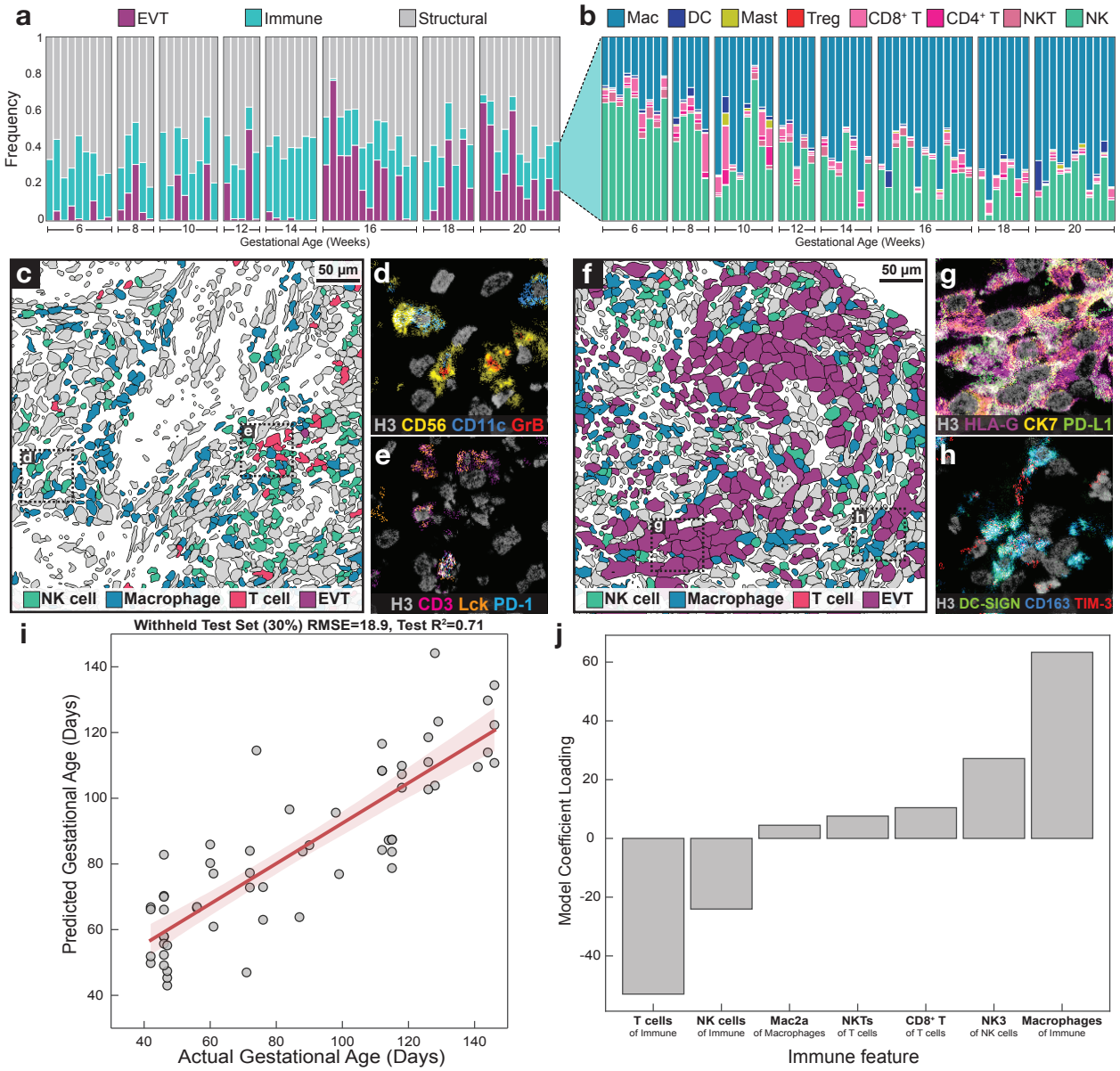

Figure 4 | A lymphoid-to-myeloid shift in immune-compartment composition is tightly correlated with gestational age (GA). a. Frequency of EVT, immune, and structural cell populations per patient, with patients ordered by GA. **b.** Frequency of immune cell populations per patient, by GA. MAC, macrophage; NKT, NK T cells; NK, total NK cells. **c.** Representative cell phenotype map of immune composition in decidual tissue in an early (6 weeks GA) sample. Green = NK, blue = macrophage, pink = T cell, purple = EVT, grey = other. **d.** Inset of **c**, showing a MIBI color overlay of NK cells with GrB expression. Grey = H3, yellow = CD56, blue = CD11c, red = GrB. **e.** Inset of **c**, showing a MIBI color overlay of T cells with PD-1 and Lck expression. Grey = H3, pink = CD3, orange = Lck, blue = PD-1. **f.** Representative cell phenotype map of immune composition in decidual tissue in a late (16 weeks GA) sample. Green = NK, blue = macrophage, pink = T cell, purple = EVT, grey = other. **g.** Inset of **f**, showing a MIBI color overlay of EVTs (1a, 1b) with PD-L1 expression. Grey = H3, purple = HLA-G, yellow = CD56, green = PD-L1. **h.** Inset of **f**, showing a MIBI color overlay of macrophages with TIM-3 expression. Grey = H3, green = DC-SIGN, blue = CD163, red = TIM-3. **i.** Predicted versus actual GA in days for a ridge regression model trained on GA-associated immune features, for a withheld test set (30%). Shaded region; 1 standard deviation. **j.** Ridge regression model coefficient loadings for GA-associated immune features.

increase in macrophage frequency (Log_2 R^2 ratio(δ:GA) ≤ -1.2, p-value for δ ≤ $1.2e^{-8}$, Figs. 3o, 4a, b). In MIBI images at weeks 6-8 (Fig. 4c, e), show NK cells and T cells, including those exhibiting cytotoxic (Fig. 4d) and immunosuppressive (Fig. 4e) phenotypes, greatly outnumbered macrophages of all subsets (Fig. 4b, c). Contrastingly, images from weeks 16-20 were dominated by interstitial EVTs (Figs. 4a, 4f-g) and an accompanying increase in tolerogenic macrophage populations (Fig. 4h) in relation to NK and T cells. To further evaluate this relationship, we asked whether immune cell composition in the decidua alone could be used to predict GA. Selecting immune features that were found to be preferentially associated with GA rather than SAR (Fig. 3o), we trained and validated a ridge regression model on a per-image basis using a random 70/30 test-train split (Extended Data Fig. S4a). Remarkably, the trained model predicted GA in the withheld test set within 19 days of the ground-truth value (R^2=0.7, Fig. 4i). On inspecting the model weights, we found that the relative contribution of decidual immune cells was consistent with the observed shift in the proportion of myeloid and lymphoid cells. In particular, the relative frequencies of T and NK cells were negatively correlated with GA, while total macrophage frequency was positively correlated with GA (Fig. 4j). Notably, a modified regression model for predicting SAR (δ) based on the same immune cell population parameters performed poorly (R^2=0.05, RMSE=0.85, Extended Data Fig. S4b), reinforcing our hypothesis that these immune correlates are driven by GA and not SAR.

Coordinated up-regulation of tolerogenic functional markers with GA

Having examined the influence of GA and SAR in driving changes in the frequency

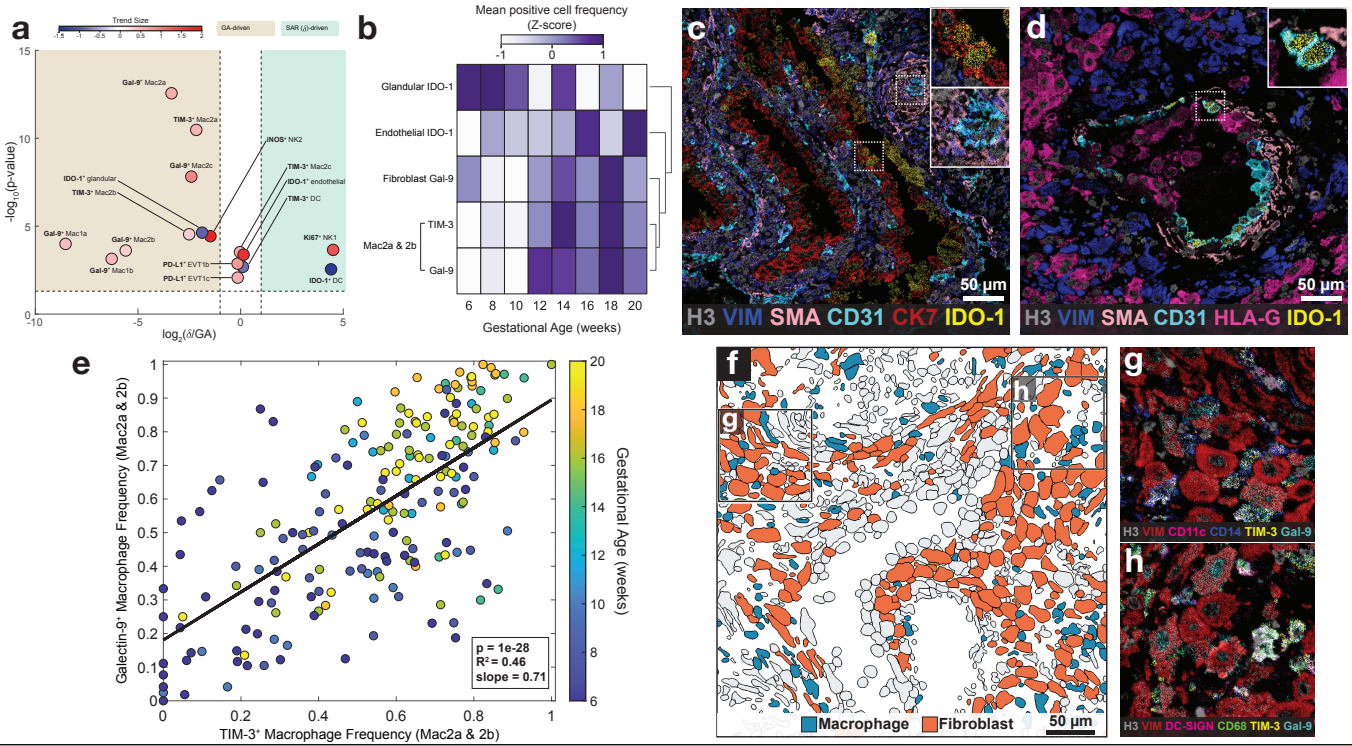

Figure 5 | Coordinated up-regulation of tolerogenic functional markers with gestational age (GA). a. Volcano plot distinguishing GA-driven from SAR (δ)-driven cell type-specific functional marker positivity fraction. X axis: $\log_2$ ratio of trend size is a relative measurement of R^2 derived from linear regression against GA or SAR (δ) and GA. Y axis: $-\log_{10}$ of the p-value for the better-fitting regression model. Points are color coded by the trend size observed in the better-fitting regression model **b.** Heatmap of changes in a subset of GA-driven functional markers as a function of GA in weeks. **c.** MIBI color overlay of IDO-1 expression in glandular cells (top inset) and endothelial cells (bottom inset) in an early (6 weeks GA) sample. Grey = H3, blue = VIM (vimentin), peach = SMA (smooth muscle actin), cyan = CD31, red = CK7, yellow = IDO-1. **d.** MIBI color overlay of IDO-1 expression in endothelial cells (inset) in spiral artery (SAR manual Stage 4) of a late (16 weeks GA) sample. Grey = H3, blue = vimentin, peach = SMA, cyan = CD31, magenta = HLA-G, yellow = IDO-1. **e.** Per-image Mac2a and Mac2b TIM-3$^+$ cell frequency versus Mac2a and Mac2b galectin-9$^+$ frequency, colored by GA. **f.** Cell phenotype map of macrophages and decidual fibroblasts. **g.** Inset of **f**; MIBI color overlay of TIM-3$^+$ and galectin-9$^+$ Mac2b and fibroblast cells. **h.** Inset of **f**; MIBI color overlay of TIM-3$^+$ and galectin-9$^+$ Mac1a, Mac1b, Mac2a, and fibroblast cells. Grey = H3, red = vimentin, pink = DC-SIGN, green = CD68, yellow = TIM-3, turquoise = Galectin-9.

of cell populations in the decidua, we next employed a similar approach to understand how these two time axes correlate with shifts in decidual function. Using the same method as our analysis of cell frequencies, we classified the temporal dynamics of functional markers expression as GA-driven, SAR-driven, or synchronized (comparably correlated with both GA and SAR) (Fig. 3o). Out of the 48 cell population-functional marker combinations that were evaluated, 16 exhibited functional marker expression that significantly correlated with one or both of these axes (Fig. 5a, see Methods, Supplementary Table 8). These data revealed three overarching trends. First, both SAR

330 and GA are associated with dynamic changes in IDO-1 expression. For example, we
331 identified a GA-driven decline in IDO-1$^+$ glandular cells (Log_2 R^2 ratio(δ:GA) = -1.8, p-
332 value for GA = $2.3e^{-5}$), a SAR-driven decline in IDO-1$^+$ dendritic cells (Log_2 R^2 ratio(δ:GA)
333 = 4.4, p-value for δ = $3e^{-3}$), and an increase in IDO-1$^+$ vascular endothelium (p-value =
334 $4e^{-4}$,Fig. 5c, d) that was comparably correlated with both GA and SAR (Fig. 5b, d).
335 Second, consistent with the cell frequency analysis (Fig. 3o) in which NK1 exhibited a
336 frequency increase preferentially associated with SAR, NK1 also exhibited a SAR
337 dependent increase in Ki67$^+$ frequency (Log_2 R^2 ratio(δ:GA) = 4.5, p-value for δ = $2e^{-4}$)
338 becoming more proliferative as arterial remodeling progresses (Fig. 5a). Third, functional
339 shifts in innate immunity were preferentially correlated with GA. All five macrophage
340 populations upregulated either TIM-3 and/or its cognate ligand Galectin-9 with GA (Fig.
341 5a, b). This trend was most prominent in the Mac2a and Mac2b populations, where a
342 tightly correlated up-regulation of both TIM-3 and Galectin-9 occurred (Fig. 5e-h,
343 Extended Data Fig. S5a). Interestingly, Galectin-9 upregulation was also detected in
344 fibroblasts (Fig. 5b, f-h). Notably, TIM-3 and Galectin-9 have been implicated in
345 suppressing anti-tumor surveillance by impairing the activity of cytotoxic NK and T cells
346 in various human cancers[30,45–47]. Taken with the SAR-driven decline in the proportion of
347 the cytotoxic NK2 observed here (Fig. 3o), these findings may suggest that TIM-3$^+$
348 Galectin-9$^+$ macrophages are serving a similar tolerogenic role in decidua.

349 Spatio-temporal EVT distribution suggests that intravasation is the predominant 350 route of EVT invasion in superficial decidua

351 Although intravascular EVTs are known to originate from the cytotrophoblast cell
352 columns, their path of migration remains a subject of debate primarily revolving around
353 two models: intravasation and extravasation (Fig. 6a). In the intravasation model, EVTs
354 detach from the cell columns and migrate through the decidua to first localize around the
355 spiral arteries. These perivascular EVTs then enter spiral arteries by migrating through
356 the arterial wall. In contrast, in the extravasation model, EVTs do not traverse the arterial
357 wall from within the decidua. Instead, detaching EVTs migrate retrograde against arterial
358 blood flow after entering at the basal plate where spiral arteries empty and merge into the
359 intervillous space[9].

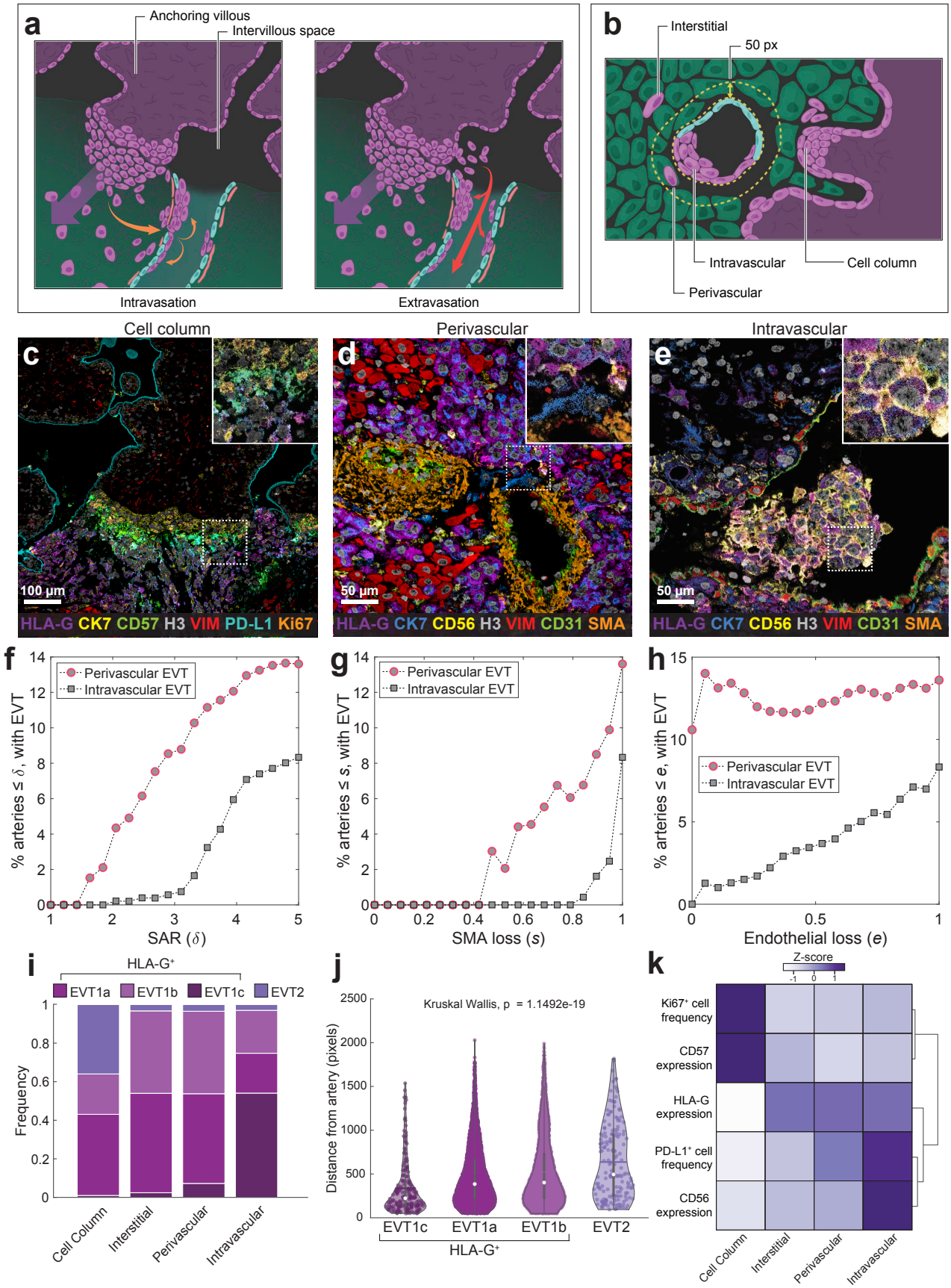
a
Anchoring villous
Intervillous space
Intravasation
Extravasation
b
Interstitial
50 px
Intravascular
Cell column
Perivascular
Cell column
Perivascular
Intravascular
c
100 µm
HLA-G CK7 CD57 H3 VIM PD-L1 Ki67
d
50 µm
HLA-G CK7 CD56 H3 VIM CD31 SMA
e
50 µm
HLA-G CK7 CD56 H3 VIM CD31 SMA
f
Perivascular EVT
Intravascular EVT
% arteries ≤ δ, with EVT
SAR (δ)
g
Perivascular EVT
Intravascular EVT
% arteries ≤ s, with EVT
SMA loss (s)
h
Perivascular EVT
Intravascular EVT
% arteries ≤ e, with EVT
Endothelial loss (e)
i
HLA-G+
EVT1a
EVT1b
EVT1c
EVT2
Frequency
Cell Column
Interstitial
Perivascular
Intravascular
j
Kruskal Wallis, p = 1.1492e-19
Distance from artery (pixels)
EVT1c
EVT1a
EVT1b
EVT2
HLA-G+
k
Z-score
Ki67+ cell frequency
CD57 expression
HLA-G expression
PD-L1+ cell frequency
CD56 expression
Cell Column
Interstitial
Perivascular
Intravascular

Figure 6 | Spatiotemporal EVT distributions suggest that intravasation is the predominant route of EVT invasion in superficial decidua. a. Two hypotheses for intravascular EVT invasion. (Left) Intravasation: orange arrows indicate movements of EVTs from the cell column of the anchoring villi into the decidua and through the wall of the artery and into the lumen. (Right) Extravasation: red arrows indicate movement of EVTs from the fetal villi through the intervillous space into the artery. **b.** Anatomical locations of interstitial, intravascular, perivascular, and cell column EVT populations in the decidua. **c.** MIBI overlay of anchoring villous and associated cell column EVT populations. Inset: cell column EVTs. Purple = HLA-G, yellow = CK7, green = CD57, grey = H3, red = VIM (vimentin), cyan = PD-L1, orange = Ki67 **d.** MIBI overlay of spiral arteries and associated perivascular EVT populations. Inset: perivascular EVT breaching artery wall. Purple = HLA-G, blue = CK7, yellow = CD56, grey = H3, red = VIM, green = CD31, orange = SMA (smooth muscle actin). **e.** MIBI overlay of remodeled spiral arteries and associated intravascular EVT populations. Inset; intravascular EVTs in a clump. Purple = HLA-G, blue = CK7, yellow = CD56, grey = H3, red = VIM, green = CD31, orange = SMA. **f.** Percentage of arteries with scores less than or equal to a given SAR (δ) threshold, by perivascular or intravascular EVTs present. **g.** Percentage of arteries with scores less than or equal to a given SMA loss (s) threshold, by perivascular or intravascular EVTs present. **h.** Percentage of arteries with scores less than or equal to a given endothelial loss (e) threshold, by perivascular or intravascular EVTs present. **i.** Frequency of EVT populations by anatomical location. **j.** Violin plot of distance from artery (in pixels) of EVTs grouped by EVT type. **k.** Heatmap of lineage and functional marker trends of EVT populations by anatomical location. Lineage marker (CD57, HLA-G, CD56) trends are mean expression values of EVT populations. Functional marker (Ki67, PD-L1) trends are the mean positive cell frequencies of EVT populations. Rows are z-scored and hierarchically clustered.

To determine which model best explains arterial invasion, we used our spatio-temporal atlas to quantify how the phenotype and spatial distribution of EVTs evolve with respect to SAR. First, we manually defined feature masks demarcating cell column anchoring villi and three decidual compartments—interstitial, perivascular, and intravascular in our images (Fig. 6b) —to quantify EVT frequency in each (Fig. 6c-e). Together with our SAR temporal trajectory, we used these data to ask a question that has been qualitatively explored in previous work[20]: Where do EVTs accumulate first—in the perivascular compartment (directly proximal to arteries) or within the intravascular compartment? We quantified peri- and intravascular EVTs on a per-artery basis with respect to their remodeling score δ and found that perivascular EVTs began accumulating around less remodeled arteries in the decidua (Fig. 6f) and were consistently present at earlier remodeling stages than intravascular EVTs (median δ = 2.2 vs. 3.2, Kruskal-Wallis p-value = $5e^{-8}$, Extended Data Fig. S6a). For arteries in which both were present, the Log_2 ratio of EVTs present in these two compartments followed a continuous and smooth trend as remodeling progressed, with intravascular EVTs increasing at the expense of perivascular EVTs (R^2 = 0.5, p-value = $9e^{-12}$, Extended Data Fig. S6b). For a small number of arteries, we observed perivascular EVTs breaching the artery wall, suggesting they are in the process of invading the arterial lumen (Fig. 6d). These data are more

378 consistent with the intravasation model in which perivascular EVT are necessary before
379 intravascular EVT could appear.

380 Loss of smooth muscle and endothelium have defining roles in determining the
381 extent of SAR. Using morphometrics to quantify the extent of these concentric layers of
382 the arterial wall (see Methods), we examined how their integrity relates to EVT enrichment
383 in the perivascular and intravascular compartments. Similar to the trend seen with respect
384 to remodeling score δ, accumulation of perivascular EVTs was consistently present
385 around arteries at an earlier stage, with intravascular EVTs only appearing after 80%
386 smooth muscle loss (median smooth muscle loss for arteries with at least five
387 intravascular EVT present: 98%, Fig. 6g). Perivascular EVTs were present around
388 arteries irrespective of the degree of endothelium loss, while intravascular EVTs
389 increased with endothelium loss (Fig. 6h, linear regression on Log transformed
390 intravascular EVT as a function of endothelium loss: R^2=0.13, p-value =$3e^{-4}$) indicating
391 that endothelial disruption is a precursor to EVT entry into the arterial lumen. This
392 conclusion further supports the intravasation model, in which EVTs must transverse the
393 endothelial barrier to enter the arterial lumen.

394 Taken together, these data are consistent with a sequential process in which EVTs
395 detach from the cytotrophoblast cell columns and migrate through the decidua as
396 interstitial EVTs in order to accumulate in the perivascular compartment prior to
397 intravasation, as suggested previously[20]. To further evaluate this model, we posed the
398 following questions: Does EVT phenotype shift in a progressive manner that is consistent
399 with this stepwise intravasation model? If so, do intravascular EVTs more closely
400 resemble the cell column or perivascular compartment?

401 To answer these questions, we first compared the frequencies of the four EVT cell
402 populations within cell column, interstitial, perivascular, and intravascular masks. The
403 composition of each of these compartments shifted in a systematic manner along the
404 proposed path of migration: the cell columns consisted primarily of EVT1a, EVT1b and
405 EVT2 subsets with few $CD56^+$ EVT1c cells (99% vs. 1%). In the interstitial compartment,
406 the frequency of EVT2 dropped by 11-fold while the frequency of EVT1c cells increased
407 modestly to 2.4%. EVT1c cells were further enriched within the perivascular compartment

408 (7.3%) but were most prevalent in the intravascular compartment (54%, Fig. 6i). In
409 addition, EVT1c cells were found significantly closer to arteries than EVT2 cells (Kruskal
410 Wallis p-value = $1.15e^{-19}$, Fig. 6j).

411 Comparison of functional marker expression across all subsets within each
412 masked compartment, again revealed a progressive shift in EVT phenotype that best
413 aligned with a route of invasion consistent with an intravasation model. Cell column
414 compartments were uniquely enriched for proliferative ($Ki67^+$), $CD57^+$ EVTs (Fig. 6k).
415 With decidual EVT invasion, a precipitous drop in CD57 and Ki67 expression was
416 accompanied by a progressive increase in PD-L1 that peaked in the intravascular
417 compartment (Fig. 6k). Notably, the intravascular compartment most closely resembled
418 the perivascular compartment in terms of functional marker expression (Fig. 6k,
419 perivascular 9.4% closer than interstitial to intravascular, Kruskal-Wallis p-value = $8e^{-7}$,
420 see Methods, Extended Data Fig. S6c). While the perivascular compartment is the most
421 similar to the intravascular compartment, a noticeable difference between the two
422 compartments was driven by PD-L1 and CD56 expression levels (Fig. 6k). This difference
423 stems from the highest prevalence of the $CD56^+$ PDL-1^+ EVT1c cells in the intravascular
424 compartment, which further increases with SAR (Fig. 6i, Extended Data Fig. S6d-f).

425 One potential explanation for the steep increase in EVT1c prevalence between the
426 perivascular and intravascular compartment is that arterial intravasation of perivascular
427 EVTs is accompanied by upregulation of CD56, such that EVT1a-b subsets would
428 effectively become the EVT1c subset. We therefore hypothesized that such a process
429 would involve an intermediate state between the two in which the EVT1a-b subsets
430 moderately express of CD56 en-route to the high expression observed in the EVT1c
431 subset. To test this hypothesis, we compared the average CD56 intensity of perivascular
432 and intravascular EVT1a-b EVTs on a per-artery basis (for arteries that initiated
433 remodeling: $\delta \geq 2$). This analysis detected a statistically significant increase in CD56
434 expression between the perivascular and intravascular compartment by EVT1a-b subsets
435 (sided Wilcoxon signed rank test p-value = $5e^{-3}$, Extended Data Fig. S6g). An alternative
436 explanation for the disproportionate enrichment of EVT1c within vessels is that they are
437 more proliferative. However, only 0.5% of intravascular EVT1c were $Ki67^+$ compared to
438 9.6% and 1.8% of intravascular EVT1a and EVT1b cells, respectively (Fig. 6k, Extended

439 Data Fig. S6h).

440 Note that given the observational nature of our spatiotemporal atlas, neither model
441 can be definitively ruled in or out. However, taken together these analyses best align with
442 an intravasation model in which decidual invasion of cell column EVTs is accompanied
443 by pronounced downregulation of CD57 and Ki67 and upregulation of HLA-G.
444 Perivascular accumulation of EVTs occurs early in SAR, preceding the appearance of
445 intravascular EVTs and any loss in endothelium. In this model, as the endothelial barrier
446 is lost, perivascular EVTs invade the artery lumen and upregulate CD56.

447 Discussion

448 Decidualization is a fascinating process with no other normative precedent in
449 human biology, where the structure and function of the maternal endometrium transforms
450 to promote invasion of actively dividing, genetically dissimilar placental cells. Many
451 aspects of this process are primate-specific and some, such as deep arterial invasion of
452 EVTs into the myometrium, are thought to be largely restricted to humans with some
453 evidence in great apes[14–17,48]. Given this lack of tractable and relevant animal models
454 and the inability to study decidualization prospectively, our understanding of this process
455 is immature relative to other areas of human physiology. With this in mind, we used MIBI-
456 TOF and archival human tissue to generate the first spatiotemporal atlas of the maternal-
457 fetal interface during 6-20 weeks gestation. The central focus of our study was to
458 understand how global, temporally dependent changes in decidual composition are
459 coupled to local regulation of vascular remodeling in pregnancy. While initial invasion of
460 placental EVTs is prompted by a shift towards a permissive milieu, progression of SAR is
461 dependent on subsequent migration and perivascular accumulation of EVTs, where they
462 are thought to participate in cooperative cell-cell interactions with maternal fibroblasts, NK
463 cells, and macrophages[4,5]. Thus, formation of the maternal-fetal interface is mediated by
464 global, temporally dependent queues that serve as a gating function for remodeling
465 processes that are regulated in the local tissue microenvironment.

466 With this paradigm in mind, we set out to delineate which aspects of the first half
467 of pregnancy are driven globally by GA and how this relates to SAR. To achieve this, we

468 mapped the spatial distribution, composition, and functional state of ~500,000 maternal
469 cells and fetal EVTs with respect to glands, anchoring cell column villi, and spiral arteries
470 in >200 images from 66 patients. Using LDA, image morphometrics, and expert
471 annotations, we assigned quantitative remodeling scores to every spiral artery in these
472 images. We then examined how cell frequency and function changed with respect to GA
473 and SAR. Our analysis of these changes determined GA to be the predominant driver of
474 maternal immune cell composition (Figs. 30, 4i, j). Progressive decreases in NK and T
475 cells drive a transition at 12-14 weeks GA from a lymphoid to myeloid predominant
476 decidua enriched for iNOS^{+} NK cells, IDO-1^{+} vascular endothelium, and DC-SIGN^{+}
477 macrophages that co-express TIM-3 and Galectin-9 (Figs. 4b, 5a, b). Notably, this
478 relationship between immune composition and GA was robust enough to allow us to
479 predict GA within 19 days based exclusively on immune population frequencies (Fig. 4i).

480 In contrast, all EVT subsets and only two maternal cell populations (NK1 and NK2)
481 preferentially correlated with progression of SAR. Higher remodeling scores were
482 correlated with more EVTs, more NK1s, and fewer NK2s. NK1 and NK2 primarily differ in
483 that the latter express CD57—a marker associated with a cytotoxic phenotype. Higher
484 proportions of presumptively more reactive NK2s early in SAR aligns well with previous
485 studies that have suggested that decidual NKs initiate early disruption of arterial smooth
486 muscle through secretion of GrB, MMP2, and MMP9[26,49]. Likewise, the proportional gains
487 seen here as SAR progresses of less reactive NK1s and invasive EVTs are consistent
488 with the tolerizing effects of HLA-G, which has been shown previously to decrease NK
489 cell cytotoxicity and induce production of IL-6 and IL-8 via binding of HLA-G to KIR2DL4,
490 LILRB1, and LILRB2[50,51]. Taken together, these data suggest that maternal and fetal cells
491 play cooperative, interdependent roles with SAR transitioning through NK- and EVT-
492 dependent phases.

493 We also examined a long-standing open question in the field: What is the path of
494 migration taken by EVTs that invade spiral arteries? On comparing cellular compositions
495 within cytotrophoblast cell columns of anchoring villi, decidua, and arteries, we found that
496 the local EVT frequency and phenotype within these regions shifted in a sequential,
497 coordinated manner consistent with an intravasation model in which EVTs within the
498 decidua enter spiral arteries through the arterial wall. Given the observational nature of

499 this study, we note that we cannot definitively rule out an extravasation model in which
500 EVTs migrate retrograde after entering spiral arteries directly at the basal plate. With this
501 limitation in mind, in our model EVTs detaching from proliferative cytotrophoblast cell
502 columns first invade the decidua and transition to a CD57- CK7^{+} HLA-G^{+} phenotype in
503 our proposed model. In line with previous work demonstrating EVT expression of MMP2
504 and MMP9[52], these cells migrate through the decidua and accumulate around spiral
505 arteries where they participate in removal of arterial smooth muscle. As this layer is
506 depleted, perivascular EVTs disrupt the underlying vascular endothelium and invade the
507 arterial lumen where they form multicellular clumps. Intravascular invasion is
508 accompanied by EVT upregulation of CD56, a homophilic binding molecule that has been
509 suggested to be necessary for heterotypic cell adhesion to endothelial cells[53]. Finally,
510 these multicellular clumps in fully remodeled arteries recede and are partially replaced by
511 trans-differentiated, endothelialized EVTs that have displaced the maternal endothelium.

512 Formation of the maternal-fetal interface is an organized and controlled invasive
513 process that is sometimes viewed as a template for understanding invasive and
514 immunosuppressive properties of tumors[54]. Both processes involve a genetically
515 dissimilar invasive cell type (haploidentical EVTs vs. clonal, mutated cancer cells),
516 extracellular matrix remodeling, and recruitment of a wide variety of tolerogenic immune
517 cells, including M2 polarized macrophages and proliferating Tregs. The intersection of
518 anchoring placental villi and maternal decidua morphologically resembles the invasive
519 margin of carcinomas and contains trophoblast cells expressing high levels of
520 immunomodulatory proteins and growth factors implicated in tumor severity including PD-
521 L1, IDO-1, TIM3, Her2, and EGFR [30,45,55,56]. In addition to these phenotypic and structural
522 similarities, recent work revealing mosaicism and clonal mutations in normal term
523 placentas demonstrate that this phenotypic overlap is even manifest at a genomic level[57].

524 Overall, we anticipate that this spatio-temporal atlas of the early human maternal-
525 fetal interface will provide a normative framework for elucidating etiological perturbations
526 in maternal-fetal tolerance and SAR in pregnancy complications. Likewise, this work may
527 also serve as a template for understanding how immune tolerance, tissue remodeling,
528 and angiogenesis are aberrantly recruited and synergized during tumor progression. With
529 this in mind, we plan in future studies to extend this comparative approach to archival

530 tissue from patients with preeclampsia, placenta accreta, and choriocarcinoma to further
531 elucidate cellular interactions involved in regulating SAR and EVT invasion.

532 Methods

533 Retrospective cohort design

534 The study cohort comprised decidua tissue from archival formalin-fixed, paraffin
535 embedded (FFPE) blocks, sampled after elective pregnancy terminations at the Women
536 Options Center at Zuckerberg San Francisco General Hospital, an outpatient clinic
537 located within a large public hospital affiliated with an academic medical center. Patients
538 at this clinic reflect a diverse population. The clinic serves women in the Bay Area as well
539 as referrals from California and out of state. While the patient population is predominantly
540 low-income mainly Medi-Cal patients, women of all economic backgrounds are cared for
541 at the clinic.

542 In the clinic, an ultrasound examination is performed to estimate GA, and medical
543 history is taken and logged as Electronic Medical Records ('eCW' - electronic clinical
544 works) or handwritten forms. A board-certified gynecologist reviewed medical records and
545 specifically extracted the following details: age, ethnicity, body mass index, gravidity,
546 parity, prior terminations, smoking, medications, HIV status, history of preeclampsia,
547 chronic hypertension, diabetes mellitus, renal disease, autoimmune disease, multifetal
548 pregnancy, and congenital anomalies (Supplementary Table 1). For procedures
549 occurring at less <14 weeks GA, suction aspiration is routinely used. For procedures at
550 >14 weeks GA, a combination of suction aspiration and grasping forceps is used. After
551 the procedure, tissue samples are routinely sent to pathology.

552 TMA construction

553 Regions of decidua with maternal spiral arteries, were cored and combined in two
554 TMA blocks by an experienced technician. Where possible, blocks containing the decidua
555 basalis were selected. Information on the histological characteristics of the blocks
556 retrieved, including the presence of cell column anchoring villi, is located in
557 Supplementary Table 2. The first TMA consisted of 205 cores (including three tonsil
558 cores, one endometrium core and one myometrium core) of 1 mm in diameter; the second

559 contained 86 cores of 1.5 mm in diameter. High resolution scans of each core were
560 uploaded to the Stanford Tissue Microarray Database (URL: http://tma.im/cgi-
561 bin/home.pl), a collaborative internal platform for designing, viewing, scoring, and
562 analyzing TMAs. Sequential recuts of the main experiment were stained with H&E, to aid
563 in choosing the imaging regions of interest (ROIs) and analyzing data.

564 Antibody preparation

565 Antibody staining was validated as described previously[28,58–60] . Briefly, each
566 reagent was first tested using single plex chromogenic IHC using multiple positive and
567 negative FFPE tissue controls prior to metal conjugation. Antibodies were then
568 conjugated to isotopic metal reporters as described previously[28,58–61] with the exception
569 of biotin-conjugated anti-PD-L1, for which a metal-conjugated secondary antibody was
570 used. Performance of metal conjugated antibody reagents were then tested within the
571 complete MIBI-TOF staining panel, under conditions identical to those in the main study
572 and compared with representative single plex chromogenic IHC to confirm equivalent
573 performance. Representative stains and information for each marker can be found in
574 Extended Data Fig. 1a and Supplementary Table 9 respectively. After conjugation,
575 antibodies were diluted in Candor PBS Antibody Stabilization solution (Candor
576 Bioscience). Antibodies were either stored at 4°C or lyophilized in 100 mM D-(+)-
577 Trehalose dehydrate (Sigma Aldrich) with ultrapure distilled H_2O for storage at −20°C.
578 Before staining, lyophilized antibodies were reconstituted in a buffer of Tris (Thermo
579 Fisher Scientific), sodium azide (Sigma Aldrich), ultrapure water (Thermo Fisher
580 Scientific), and antibody stabilizer (Candor Bioscience) to a concentration of 0.05 mg/mL.
581 Information on the antibodies, metal reporters, and staining concentrations is located in
582 Supplementary Table 9.

583 Tissue staining

584 Tissues were sectioned (4 μm in thickness) from tissue blocks on gold and
585 tantalum-sputtered microscope slides. Slides were baked at 70°C for 20 minutes followed
586 by deparaffinization and rehydration with washes in xylene (3x), 100% ethanol (2x), 95%
587 ethanol (2x), 80% ethanol (1x), 70% ethanol (1x), and ddH_2O with a Leica ST4020 Linear
588 Stainer (Leica Biosystems). Tissues next underwent antigen retrieval was carried out by

589 submerging sides in 3-in-1 Target Retrieval Solution (pH 9, DAKO Agilent) and incubating
590 them at 97°C for 40 minutes in a Lab Vision PT Module (Thermo Fisher Scientific). After
591 cooling to room temperature slides were washed in 1x PBS IHC Washer Buffer with
592 Tween 20 (Cell Marque) with 0.1% (w/v) bovine serum albumin (Thermo Fisher). Next,
593 all tissues underwent two rounds of blocking, the first to block endogenous biotin and
594 avidin with an Avidin/Biotin Blocking Kit (Biolegend). Tissues were then washed with wash
595 buffer and blocked for 1 hour at room temperature with 1x TBS IHC Wash Buffer with
596 Tween 20 with 3% (v/v) normal donkey serum (Sigma-Aldrich), 0.1% (v/v) cold fish skin
597 gelatin (Sigma Aldrich), 0.1% (v/v) Triton X-100, and 0.05% (v/v) Sodium Azide. The first
598 antibody cocktail was prepared in 1x TBS IHC Wash Buffer with Tween 20 with 3% (v/v)
599 normal donkey serum (Sigma-Aldrich) and filtered through a 0.1 µm centrifugal filter
600 (Millipore) prior to incubation with tissue overnight at 4°C in a humidity chamber. After the
601 overnight incubation slides were washed for 2 minutes in wash buffer. The second day,
602 the antibody cocktail was prepared as described (Supplementary Table 9) and incubated
603 with the tissues for 1 hour at 4°C in a humidity chamber. After staining, slides were
604 washed twice for 5 minutes in wash buffer and fixed in a solution of 2% glutaraldehyde
605 (Electron Microscopy Sciences) solution in low-barium PBS for 5 minutes. Slides were
606 washed in low-barium PBS for 20 seconds then, using a linear stainer, through 0.1 M Tris
607 at pH 8.5 (3x), ddH2O (2x), and then dehydrated by washing in 70% ethanol (1x), 80%
608 ethanol (1x), 95% ethanol (2x), and 100% ethanol (2x). Slides were dried under vacuum
609 prior to imaging.

610 MIBI-TOF imaging

611 Imaging was performed using a custom MIBI-TOF instrument with a Xe+ primary
612 ion source, as described previously[28,61]. 222 808 x 808um Fields of View (FOVs) were
613 acquired at approximately 600 nm resolution using an ion dose of 7nA*hr/mm^2. After
614 excluding 11 FOVs that contained necrotic or non-decidual tissue, or consisted of
615 duplicate tissue regions, the final dataset consisted of 211 FOVs from 66 patients.

616 Low-level image processing

617 Multiplexed image sets were extracted, slide background-subtracted, denoised,
618 and aggregate filtered as previously described[35,59–61]. For several markers, a

619 “background” channel consisting of signal from the mass 128 channel was used. All
620 parameters used as inputs for low-level processing are listed in Supplementary Table 9.

621 ## Feature annotation

622 Large tissue features were manually annotated in collaboration with a perinatal
623 pathologist. Pseudo-colored MIBI images with H3 to identify cell nuclei, vimentin for
624 decidual stromal cells, smooth muscle actin and CD31 for vessels, cytokeratin 7 (CK7)
625 for glands and the fetal cell columns, and HLA-G for EVTs were used to guide annotation.
626 Serial H&E sections, and an H&E recut of the entire block, if necessary, were additionally
627 used to supplement annotation. Labelling was performed in ImageJ and the annotated
628 features were exported as binary TIF masks.

629 ## Single cell segmentation

630 The Mesmer segmentation algorithm[36] was adapted specifically to segment the
631 cells in our dataset. First, training data were generated using a subset of 15 images out
632 of 211 in our cohort, in addition to 10 decidua MIBI-TOF images from titration data. 1024
633 x 1024 pixel crops were selected to encompass the range of different cell morphologies
634 present. The markers H3, vimentin, HLA-G, CD3, CD14 and CD56 were used to capture
635 the major cell lineages present. Subsequently, a team of annotators parsed these images
636 to identify the location of each unique cell using DeepCell Label, custom annotation
637 software specifically developed for this task[36] (code URL:
638 https://github.com/vanvalenlab/deepcell-label). The manually annotated images were
639 used to generate partially overlapping crops of 256 x 256 pixels from each image. In total,
640 training data included 1600 distinct crops with 93,000 cells. This dataset was used to
641 retrain the Mesmer segmentation model, modifying the architecture to accept six distinct
642 channels of input. The output from the network was then post-processed using the default
643 model settings (Extended Data Fig. S2a).

644 ## Segmentation post-processing

645 Examination of the images revealed that glandular cells and chorionic villus
646 trophoblasts did not express any markers included in the training data; namely these cells
647 were predominantly $CK7^{+}$. This resulted in effectively nuclear-only segmentation being

648 predicted by the CNN within these features. To account for this, segmented cells that
649 overlapped with the gland mask were expanded radially by 5 pixels, and those in the cell
650 column mask by 2 pixels. This approach accounted for glandular cells and cell column
651 anchoring trophoblasts that were not expressing any markers but were included in the
652 training data, resulting in effectively nuclear-only segmentation being predicted by the
653 convolutional neural network. The number of pixels used for expansion was optimized to
654 approximate the observed cell size, based on systematic inspection of three images per
655 GA.

656 ## Single-cell phenotyping and composition

657 Single cell expression data were extracted for all cell objects and area-normalized.
658 Objects <100 pixels in area were deemed noncellular and excluded from subsequent
659 analyses. Single-cell data were linearly scaled with a scaling factor of 100 and ArcSinh-
660 transformed with a co-factor of 5. All mass channels were normalized to the 99th
661 percentile. To assign decidual cell populations (≥ 70% cell area in decidua) to a lineage,
662 the clustering algorithm FlowSOM (Bioconductor "FlowSOM" package in R)[37] was used,
663 which separated cells into 100 clusters based on the expression of 19 canonical lineage
664 defining markers (Extended Data Fig. S2b). Clusters were further classified into 21 cell
665 populations, with proper lineage assignments ensured by manual examination of
666 overlayed FlowSOM cluster identity with lineage-specific markers. Clusters containing
667 non biologically meaningful or distinct signals were assigned the label 'other'. Tregs were
668 identified by thresholding T cells (FlowSOM clusters 43, 53, 63) with CD3 signal ≥ the
669 mean CD3 expression of $CD4^+$ T cells and > 0.5 normalized expression of FOXP3. Mast
670 cells were identified as cells for which normalized expression of tryptase was >0.9. Mac2b
671 ($CD11c^+$) cells were identified as macrophages with >0.5 normalized expression of
672 CD11c. Placental macrophages (Hofbauer cells) were defined as $CD14^+$ >0.5 cells
673 located within the cell column. Cells from FlowSOM clusters 4, 5, and 15 ubiquitously and
674 predominantly expressed CK7 and were reassigned to the EVT2 subset if located within
675 the cell column feature mask, or as glandular cells otherwise (Extended Data Fig. S2b).
676 These thresholds were selected based on the distribution of lineage marker expression
677 (Extended Data Fig. S2c) as well as on systematic examination of the images by eye

678 since expression patterns varied significantly between markers.

679 Definition of thresholds for functional marker positivity

680 Cells were considered positive for a functional marker if their scaled expression
681 level was ≥ a set threshold, as described previously[61]. Thresholds for individual functional
682 markers were determined based on the distribution of functional marker expression and
683 by examining the images by eye, as expression patterns varied significantly between
684 markers (Extended Data Fig. S2e, Supplementary Table 4). To set the per marker
685 thresholds, 5 images for each functional marker were reviewed and increasing threshold
686 values were examined using custom software. Subsequently, cells defined as negative
687 for a marker based on the determined threshold value were re-examined to ensure the
688 thresholds were representative. For Ki67 positivity, only cells that had a nucleus in the
689 image were considered. Ki67 values were not cell size normalized because the Ki67
690 signal is exclusive to nuclei.

691 Blinded manual artery staging

692 Arteries were categorized into 5 remodeling stages based on criteria adapted from
693 the 4-stage model proposed by Smith et al[42]. These criteria were previously used to
694 describe spiral arteries observed in H&E and single channel IHC images and were
695 adapted to suit multiplexed MIBI data (Fig. 3a, details in Extended data Fig. S3a). 600
696 arteries were categorized according to these criteria by a single reviewer using
697 exclusively crops of MIBI pseudocolor overlays (SMA, Vimentin, CD31, H3, and HLA-G)
698 including only the artery (as defined by feature mask) and any EVTs in the lumen. The
699 reviewer was blinded to the rest of the image, serial H&E sections, gestational age, and
700 any clinical data. 12 partially captured arteries were excluded from the final dataset of
701 588 arteries.

702 Automated digitization of artery morphological features

703 The same format of cropped artery MIBI images that were manually scored by the
704 reviewer were used to calculate a set of geometric parameters for several selected
705 features. These features described the organization and structure of the vessel wall, the
706 continuity of the endothelium and its thickness, and the presence and structure of

intravascular EVTs. In order to capture these features, a structure of concentric circles we termed the “onion” structure is defined, with the outer circle of this structure enclosing the artery and the inner circles dividing it into layers. This structure is described below using the two-dimensional cylindrical coordinate system with the radial axis r, azimuthal (angular) axis ø, and origin of the axis at point (x,y). Point (x,y) is the user defined artery center. For an artery in the binary mask M, the following algorithm was used to create the “onion” structure (Extended Data Fig. S3c):

- Define a circle enclosing the artery, centered at point (x,y) with radius a as follows:
  - (x,y) was taken as the user-defined artery center point
  - a, the radius is defined as the maximum distance between (x,y) and the edge of M – rounded up to the nearest integer multiple of n, such that a=I*n for an integer I. n is a user defined thickness parameter for the “onion” layers.
- Define the inner circles comprising the “onion” layers:
  - Divide the radius a of the outer circle into I equal sections of length n, creating layers along the radial r axis.
  - The radii of the inner circles are then defined as: 0,1*n,2*n,…(I-1)*n.
- Divide the “onion” into k equal sectors along the ø axis, k is a user defined integer.
- Subdivide each sector into segments:
  - The sectors are internally divided by the circles, creating parts with 4 corners and 4 sides, with the 2 sides being straight (sector dividers), and the 2 sides being arcs (parts of ellipse circumferences).
  - The arcs are replaced with secants (straight line connecting the ends of the arc), turning the segment into a trapezoid.
  - The parameters n=10 pixels and k=100 were used to allow for segments large enough to contain a sufficient number of pixels to average expression over.

The following features are then extracted for each artery “onion”:

1. Geometrical features:
   a. radius - the maximum distance between any pixel within the mask and the

closest pixel on the edge of the mask.

b. perimeter – the Euclidean distance between all adjacent pixels on the edge of the artery mask

c. area – the total number of pixels within the artery mask

2. Protein morphology features, for each of the following markers: CD31, CK7, H3, HLA-G, SMA, VIM

   a. Average signal – weighted-average over segments of marker expression, where the weight of a segment corresponds to the number of pixels it contains. Weighted average was used to avoid smaller inner segments having disproportionate effect on the average.

   b. Thickness –

      i. For each sector we calculate the distance d between the inner-most segment positive for the marker and the outer-most positive segment. Positivity is measured by comparing the mean signal over pixels the segment to a user defined threshold.

      ii. The mean and standard deviation of thickness are calculated as the mean and standard deviation of d over all sectors.

   c. Radial coverage - the percentage of sectors positive for marker signal. A sector is considered positive if the mean signal over sector pixels accedes a user defined threshold.

   d. Jaggedness – This feature measures the extent jaggedness of an artery outline. To do so, first a skeletonization function written by Nicholas R. Howe [62] is applied to the artery mask, this function returns a “skeleton” of the artery outline. This “skeleton” also assigns values to the outline pixels based on their distance from the core shape. Then, two different binarization thresholds are chosen: a “non- branch” threshold (a high value = 60 pixels, indicating greater topological distance and a “branch” threshold (a low value = 5 pixels, indicating smaller topological distance). The ratio between the total number of “non branch” and “branch” pixels is the jaggedness.

767 ## Calculation of continuous SAR remodeling score δ

768 A supervised dimensionality reduction technique based on linear discriminant
769 analysis (LDA)[43] (code URL: https://github.com/davidrglass) was employed using the per
770 artery digitized morphological features and manually assigned remodeling stage labels
771 as inputs. All artery morphology feature values were standardized (mean subtracted and
772 divided by the standard deviation) and all arteries were used as training data. The LDA
773 output was:

774 a. The optimal linear combination of a subset of features, that maximized the
775 separation by manual stage between arteries in LDA space (Supplementary Table
776 6)
777 b. The coordinates of each artery in LDA space (Supplementary Table 5)

778 In order to define the SAR trajectory, a fourth-degree polynomial was fitted to the
779 artery coordinates in LDA space. To determine the optimal degree of the polynomial,
780 polynomials with degrees 1-6 were fitted and the degree that minimized the p-value for
781 separating δ distributions between arteries grouped by manual remodeling stage
782 (Extended Data Fig. S3f) was selected. The polynomial fit was implemented using the
783 MATLAB function fit and resulted in the following polynomial: $f(x) = 0.0005*x^4 -0.01227*x^3$
784 $+ 0.1363*x^2 -0.4354*x -0.7425$. The polynomial was then numerically interpolated on a
785 dense 10^4 point grid and the distance from each artery point in LDA space to the
786 polynomial was calculated using this grid and the MATLAB exchange function
787 distance2curve [63]. δ per artery was then calculated as the line integral from the curve
788 origin to closest point to the artery on the curve (Fig. 3n, inset). This integral was
789 numerically calculated using a custom MATLAB script. δ values were linearly rescaled to
790 the range 1-5 using the MATLAB function rescale.

791 ## Cell type frequency as function of GA and SAR

792 For examining cell type frequencies within the decidua as function of GA and SAR
793 (Fig. 3, Fig. 4), per image cell frequency tables were constructed in which cell type
794 frequencies were calculated as the proportion of cells in the decidua feature mask of that
795 image. Cells located in other feature masks (artery, gland, vessel, or cell column masks)
796 were not counted, nor were cells of an unassigned type ('other'). In order to focus these

797 analyses on cell populations strictly found in the decidua, muscle and glandular cells were
798 also excluded; these cell types occasionally extended outside of their artery and gland
799 feature masks, respectively. Cell frequency as a function of GA for a cell type was defined
800 as the per image proportion values for that cell type, as function of the GAs associated
801 with the images. Similarly, cell frequency as a function of SAR for a cell type was defined
802 as the per image proportions of that cell type, as function of the mean δ values per image.
803 For the volcano plot in Fig. 3o, we fitted a linear regression model to the two above-
804 described functions. All linear regression models were implemented using the MATLAB
805 function fitlm and the volcano plot only shows points for which regression $R^2 \geq 0.05$. R^2
806 and p-values for all δ and GA based regressions can be found in Supplementary Table
807 7. The ration between R^2 in the two regression models was used to classify trends as GA-
808 driven, SAR-driven or synchronized. For example, the increase in EVTs out of all cells,
809 R_EVT, was classified as GA-driven because R^2 for R_EVT as a function of δ was 0.3,
810 but only 0.1 for R_EVT as a function of GA (Extended Data Figure S3g, Supplementary
811 Table 7). Another example is the increase in macrophages out of immune cells,
812 I_sumMac: it was classified as GA-driven since R^2 for I_sumMac as a function of GA was
813 0.6 but only 0.1 for I_sumMac as a function of δ (Extended Data Figure S3f,
814 Supplementary Table 7). For determining trend sizes depicted in Fig. 3o, the following
815 calculation was used: denote the per image frequencies of a cell type as V, and the
816 corresponding per image temporal stamps (either GA or mean image δ) as X. Trend size
817 is then calculated as the difference between the first and last time point in units of the
818 mean: $\frac{V(\max(X)) - V(\min(X))}{mean(V)}$.

819 Functional markers positivity rate per cell type as function of GA and SAR

820 For examining cell type specific temporal trends in the expression of functional
821 markers (Fig. 5a), 48 combinations of cell type- functional marker were selected. The
822 selected combinations were those for which the positivity frequency Z-score exceeded
823 0.5 (Fig. 2a, right panel). For each of these combinations, the frequency of cells positive
824 for the functional marker was calculated as the number of cells positive for the marker
825 (see "Definition of thresholds for functional marker positivity"), out of the total number of
826 cells of the same cell type in the image. All cells except those located within the cell

827 column mask were included to focus the analysis on functional marker trends of maternal
828 cells and EVTs that had infiltrated the decidua. For glandular cells, the location was further
829 restricted to the glands mask. The frequency of cells positive for a functional marker as a
830 function of GA, for a cell type, was defined as the per image positivity proportion values
831 as function of the GAs associated with the images. Similarly, marker positivity frequency
832 as a function of SAR for a cell type was defined as the per image proportions of that cell
833 type positive for the marker, as function of the mean δ values per image. For the volcano
834 plot in Fig. 5a, we fitted a linear regression model to the two above-described functions.
835 All linear regression models were implemented using the MATLAB function fitlm and the
836 volcano plot only shows points for which regression $R^2 \geq 0.05$. R^2 and p-values for all δ
837 and GA based regressions can be found in Supplementary Table 8. For determining trend
838 sizes depicted in Fig. 5a, the following calculation was used: denote the linear fit to the
839 per-image marker positivity proportion of a cell type as V, and the corresponding per
840 image temporal stamps (either GA or mean image δ) as X. Trend size is then calculated
841 as the difference between the first and last time point in units of the mean:
842 $\frac{V(\max(X)) - V(\min(X))}{mean(V)}$.

843 Ridge regression for predicting GA from immune composition

844 Ridge regression was implemented using the sklearn Python package
845 (sklearn.linear_model.Ridge, RidgeCV). Per-image immune frequencies were rescaled to
846 the range 0-1 prior to model fitting, using the sklearn scaling function. Images with fewer
847 than 10 immune cells were excluded (n=8). A randomly derived test-train split of 30/70
848 was used and GA distribution was verified to be equally represented in the test and train
849 sets (Extended Data Fig. S4a). Ridge regression adds a regularization penalty to the loss
850 function in order to prevent over or under representation of correlated variables, such as
851 immune cell populations. The penalty used for the test set (0.81) was selected using
852 Leave-One-Out Cross-Validation on the training set.

853 Definition of anatomical EVT location and associated arteries

854 Cell column EVTs were defined as EVTs located within cell column masks,
855 intravascular EVTs were located within artery masks, and interstitial EVTs were located

856 in the decidua. Perivascular EVTs were defined as interstitial EVTs located within 50
857 pixels of the edge of an artery, as defined by radial expansion of the artery masks (Fig.
858 6b). Arteries were said to have perivascular or intravascular EVT (Figs. 6f-h) if the number
859 of EVT in the appropriate artery compartment was $\geq$5. For Fig. 6j, only images that
860 contained all four EVT types were considered and cell to artery distance was measured
861 from the cell centroid as detected by segmentation to the border of the artery mask. For
862 Fig. 6i, one image was excluded (16_31762_20_8) due to abnormal tissue morphology.

863 ## SMA and endothelium loss scores

864 The loss scores presented in Fig. 6g, h were based on digitized morphological
865 features. For SMA, the average feature was used and for endothelium, the radial
866 coverage of CD31 (see "Automated digitization of artery morphological features"). The
867 values for each of the two features were then divided by their maximum across arteries
868 and subtracted from 1 to obtain a loss score. The resulting values were then linearly
869 rescaled to the range 0-1 using the MATLAB function rescale.

870 ## LDA of EVTs by compartment

871 A method similar to our calculation of the continuous SAR remodeling score δ was
872 used for compartment-wise analysis of EVT types. The input table consisted of marker
873 expression values per EVT. Lineage and functional markers expressed by EVTs were
874 included: CD56, CD57, HLA-G, CK7, PD-L1 and Ki67 (Fig. 2a). EVTs were labeled by
875 spatial compartment: cell column, interstitial, perivascular or intravascular (see "Definition
876 of anatomical EVT location"). Marker expression values were standardized (mean
877 subtracted and divided by the standard deviation) and cell column, interstitial, and
878 intravascular location labels per EVT were used for training the LDA model. Perivascular
879 EVTs were withheld as a test set. Due to the small number or features (markers) a one-
880 dimensional LDA was calculated yielding a single coordinate LD1. LD1 was the optimal
881 linear combination of a subset of markers, to maximize the separation by compartment
882 between EVTs (Supplementary Table 10). LD1 values were subsequently calculated for
883 the withheld test set of perivascular EVTs (Supplementary Table 11). To calculate the
884 difference in similarity to intravascular EVT between interstitial and perivascular, the
885 following calculation was used: intravascular-perivascular similarity was defined as

886 $sim_{intra-peri} = mean(Ld1_{intravascular}) - mean(Ld1_{perivascular})$. Similarly, intravascular-
887 interstitial similarity was defined as $sim_{intra-inter} = mean(Ld1_{intravascular}) -$
888 $mean(Ld1_{interstitial})$. The difference in these similarities was then calculated as:
889 $\frac{sim_{intra-inter} - sim_{intra-peri}}{im_{intra-inter}}$ in %.

890 ## Statistical analyses

891 Throughout the paper, the Kruskal-Wallis test was implemented using the
892 MATLAB function KruskalWallis. All linear regression models were implemented using
893 the MATLAB function fitlm unless stated otherwise. The sided Wilcoxon signed rank test
894 for paired analysis in Extended Data Fig. S6 was implemented using the MATLAB
895 function signrank. MATLAB version used throughout the paper for statistical analysis is
896 MATLAB 2020b.

897 ## Data availability

898 Imaging data, segmentation masks, and extracted features will be made publicly
899 available prior to publication. Code is currently available upon request and will be made
900 public prior to publication.

901 # References

902 1. Moffett-King, A. Natural killer cells and pregnancy. *Nature reviews. Immunology* **2**,
903 656–663 (2002).

904 2. Red-Horse, K. *et al.* Trophoblast differentiation during embryo implantation and
905 formation of the maternal-fetal interface. *The Journal of clinical investigation* **114**,
906 744–754 (2004).

907 3. Menkhorst, E., Winship, A., van Sinderen, M. & Dimitriadis, E. Human extravillous
908 trophoblast invasion: intrinsic and extrinsic regulation. *Reproduction, fertility, and*
909 *development* **28**, 406–415 (2016).

910 4. Vento-Tormo, R. *et al.* Single-cell reconstruction of the early maternal–fetal
911 interface in humans. *Nature* **563**, 347–353 (2018).

912 5. Suryawanshi, H. *et al.* A single-cell survey of the human first-trimester placenta and

913 decidua. *Science Advances* **4**, eaau4788 (2018).

914 6. Mor, G., Aldo, P. & Alvero, A. The unique immunological and microbial aspects of
915 pregnancy. *Nature reviews. Immunology* **17**, 469–482 (2017).

916 7. Kam, E. P. Y., Gardner, L., Loke, Y. W. & King, A. The role of trophoblast in the
917 physiological change in decidual spiral arteries. *Human Reproduction* **14**, (1999).

918 8. Whitley, G. S. J. & Cartwright, J. E. Cellular and Molecular Regulation of Spiral
919 Artery Remodelling: Lessons from the Cardiovascular Field. *Placenta* **31**, 465–474
920 (2010).

921 9. Pijnenborg, R., Vercruysse, L. & Hanssens, M. The Uterine Spiral Arteries In
922 Human Pregnancy: Facts and Controversies. *Placenta* vol. 27 939–958 (2006).

923 10. Kliman, H. J. Uteroplacental Blood Flow: The Story of Decidualization,
924 Menstruation, and Trophoblast Invasion. *The American Journal of Pathology* **157**,
925 1759–1768 (2000).

926 11. Burton, G. J., Woods, A. W., Jauniaux, E. & Kingdom, J. C. P. Rheological and
927 Physiological Consequences of Conversion of the Maternal Spiral Arteries for
928 Uteroplacental Blood Flow during Human Pregnancy. *Placenta* **30**, 473–482
929 (2009).

930 12. Khong, T., de Wolf, F., Robertson, W. & Brosens, I. Inadequate maternal vascular
931 response to placentation in pregnancies complicated by pre-eclampsia and by
932 small-for-gestational age infants. *British journal of obstetrics and gynaecology* **93**,
933 1049–1059 (1986).

934 13. Brosens, I., Pijnenborg, R., Vercruysse, L. & Romero, R. THE “GREAT
935 OBSTETRICAL SYNDROMES” ARE ASSOCIATED WITH DISORDERS OF DEEP
936 PLACENTATION. *American Journal of Obstetrics and Gynecology* **204**, 193
937 (2011).

938 14. Carter, A. M. Animal Models of Human Placentation – A Review. *Placenta* **28**, S41–
939 S47 (2007).

940 15. Schmidt, A., Morales-Prieto, D. M., Pastuschek, J., Fröhlich, K. & Markert, U. R.

941 Only humans have human placentas: molecular differences between mice and
942 humans. *Journal of Reproductive Immunology* **108**, 65–71 (2015).

943 16. Pijnenborg, R., Vercruysse, L. & Carter, A. M. Deep trophoblast invasion and spiral
944 artery remodelling in the placental bed of the lowland gorilla. *Placenta* **32**, 586–591
945 (2011).

946 17. Pijnenborg, R., Vercruysse, L. & Carter, A. M. Deep trophoblast invasion and spiral
947 artery remodelling in the placental bed of the chimpanzee. *Placenta* **32**, 400–408
948 (2011).

949 18. Gaynor, L. M. & Colucci, F. Uterine Natural Killer Cells: Functional Distinctions and
950 Influence on Pregnancy in Humans and Mice. *Frontiers in Immunology* **0**, 467
951 (2017).

952 19. Yang, F., Zheng, Q. & Jin, L. Dynamic Function and Composition Changes of
953 Immune Cells During Normal and Pathological Pregnancy at the Maternal-Fetal
954 Interface. *Frontiers in Immunology* **10**, 2317 (2019).

955 20. Pijnenborg, R., Bland, J. M., Robertson, W. B. & Brosens, I. Uteroplacental arterial
956 changes related to interstitial trophoblast migration in early human pregnancy.
957 *Placenta* **4**, 397–413 (1983).

958 21. Chaline, J. Increased cranial capacity in hominid evolution and preeclampsia.
959 *Journal of reproductive immunology* **59**, 137–152 (2003).

960 22. Rockwell, C., Vargas, E. & Moore, L. G. Human physiological adaptation to
961 pregnancy: Inter- and intraspecific perspectives. *American Journal of Human*
962 *Biology* **15**, 330–341 (2003).

963 23. Zhu, H., Hou, C. C., Luo, L. F., Hu, Y. J. & Yang, W. X. Endometrial stromal cells
964 and decidualized stromal cells: Origins, transformation and functions. *Gene* **551**,
965 1–14 (2014).

966 24. TANG, B., GULLER, S. & GURPIDE, E. Mechanism of Human Endometrial Stromal
967 Cells Decidualization. *Annals of the New York Academy of Sciences* **734**, 19–25
968 (1994).

969 25. Moffett, A. & Colucci, F. Uterine NK cells: active regulators at the maternal-fetal
970 interface. *The Journal of clinical investigation* **124**, 1872–1879 (2014).

971 26. Robson, A. *et al.* Uterine natural killer cells initiate spiral artery remodeling in human
972 pregnancy. *The FASEB Journal* **26**, 4876–4885 (2012).

973 27. Craven, C. M., Morgan, T. & Ward, K. Decidual spiral artery remodelling begins
974 before cellular interaction with cytotrophoblasts. *Placenta* **19**, 241–252 (1998).

975 28. Keren, L. *et al.* MIBI-TOF: A multiplexed imaging platform relates cellular
976 phenotypes and tissue structure. *Science Advances* **5**, eaax5851 (2019).

977 29. Chang, R.-Q., Li, D.-J. & Li, M.-Q. The role of indoleamine-2,3-dioxygenase in
978 normal and pathological pregnancies. *American Journal of Reproductive*
979 *Immunology* **79**, e12786 (2018).

980 30. Yasinska, I. M. *et al.* The Tim-3-Galectin-9 Pathway and Its Regulatory
981 Mechanisms in Human Breast Cancer. *Frontiers in Immunology* **0**, 1594 (2019).

982 31. Li, M. *et al.* Tim-3/CTLA-4 pathways regulate decidual immune cells-extravillous
983 trophoblasts interaction by IL-4 and IL-10. *FASEB journal : official publication of the*
984 *Federation of American Societies for Experimental Biology* **35**, (2021).

985 32. Hu, X. *et al.* Newly characterized decidual Tim-3+ Treg cells are abundant during
986 early pregnancy and driven by IL-27 coordinately with Gal-9 from trophoblasts.
987 *Human reproduction (Oxford, England)* **35**, 2454–2466 (2020).

988 33. Wang, S. *et al.* Tim-3 protects decidual stromal cells from toll-like receptor-
989 mediated apoptosis and inflammatory reactions and promotes Th2 bias at the
990 maternal-fetal interface. *Scientific Reports 2015 5:1* **5**, 1–9 (2015).

991 34. Sedlmayr, P. *et al.* Localization of indoleamine 2,3-dioxygenase in human female
992 reproductive organs and the placenta. *Molecular Human Reproduction* **8**, 385–391
993 (2002).

994 35. Baranski, A. *et al.* MAUI (MBI Analysis User Interface)-An image processing
995 pipeline for Multiplexed Mass Based Imaging. *PLoS computational biology* **17**,
996 (2021).

997 36. Greenwald, N. F. *et al.* Whole-cell segmentation of tissue images with human-level
998 performance using large-scale data annotation and deep learning. *bioRxiv*
999 2021.03.01.431313 (2021) doi:10.1101/2021.03.01.431313.

1000 37. van Gassen, S. *et al.* FlowSOM: Using self-organizing maps for visualization and
1001 interpretation of cytometry data. *Cytometry Part A* **87**, 636–645 (2015).

1002 38. Faas, M. M. & de Vos, P. Uterine NK cells and macrophages in pregnancy. *Placenta*
1003 **56**, 44–52 (2017).

1004 39. Kämmerer, U. *et al.* Unique Appearance of Proliferating Antigen-Presenting Cells
1005 Expressing DC-SIGN (CD209) in the Decidua of Early Human Pregnancy. *The*
1006 *American Journal of Pathology* **162**, 887–896 (2003).

1007 40. Huhn, O. *et al.* Distinctive phenotypes and functions of innate lymphoid cells in
1008 human decidua during early pregnancy. *Nature Communications* **11**, (2020).

1009 41. Salvany-Celades, M. *et al.* Three Types of Functional Regulatory T Cells Control T
1010 Cell Responses at the Human Maternal-Fetal Interface. *Cell Reports* **27**, 2537-
1011 2547.e5 (2019).

1012 42. Smith, S. D., Dunk, C. E., Aplin, J. D., Harris, L. K. & Jones, R. L. Evidence for
1013 immune cell involvement in decidual spiral arteriole remodeling in early human
1014 pregnancy. *American Journal of Pathology* **174**, 1959–1971 (2009).

1015 43. Tsai, A. G. *et al.* Multiplexed single-cell morphometry for hematopathology
1016 diagnostics. *Nature Medicine* **26**, (2020).

1017 44. Nielsen, C. M., White, M. J., Goodier, M. R. & Riley, E. M. Functional significance
1018 of CD57 expression on human NK cells and relevance to disease. *Frontiers in*
1019 *Immunology* vol. 4 (2013).

1020 45. Gonçalves Silva, I. *et al.* The Tim-3-galectin-9 Secretory Pathway is Involved in the
1021 Immune Escape of Human Acute Myeloid Leukemia Cells. *EBioMedicine* **22**, 44–
1022 57 (2017).

1023 46. Blois, S. M. *et al.* Role of galectin-glycan circuits in reproduction: from healthy
1024 pregnancy to preterm birth (PTB). *Seminars in Immunopathology 2020 42:4* **42**,

1025 469–486 (2020).

1026 47. Blois, S. M. *et al.* Pregnancy Galectinology: Insights Into a Complex Network of
1027 Glycan Binding Proteins. *Frontiers in Immunology* **0**, 1166 (2019).

1028 48. Robillard, P. Y., Dekker, G. A. & Hulsey, T. C. Evolutionary adaptations to pre-
1029 eclampsia/eclampsia in humans: Low fecundability rate, loss of oestrus,
1030 prohibitions of incest and systematic polyandry. *American Journal of Reproductive*
1031 *Immunology* vol. 47 104–111 (2002).

1032 49. Naruse, K. *et al.* Localization of matrix metalloproteinase (MMP)-2, MMP-9 and
1033 tissue inhibitors for MMPs (TIMPs) in uterine natural killer cells in early human
1034 pregnancy. *Human Reproduction* **24**, 553–561 (2009).

1035 50. Hunt, J., Petroff, M., McIntire, R. & Ober, C. HLA-G and immune tolerance in
1036 pregnancy. *FASEB journal : official publication of the Federation of American*
1037 *Societies for Experimental Biology* **19**, 681–693 (2005).

1038 51. Tilburgs, T., Evans JH, Crespo, Â. & Strominger, J. The HLA-G cycle provides for
1039 both NK tolerance and immunity at the maternal-fetal interface. *Proceedings of the*
1040 *National Academy of Sciences of the United States of America* **112**, 13312–13317
1041 (2015).

1042 52. Isaka, K. *et al.* Expression and Activity of Matrix Metalloproteinase 2 and 9 in
1043 Human Trophoblasts. *Placenta* **24**, 53–64 (2003).

1044 53. Harris, L. K., Jones, C. J. P. & Aplin, J. D. Adhesion Molecules in Human
1045 Trophoblast – A Review. II. Extravillous Trophoblast. *Placenta* **30**, 299–304 (2009).

1046 54. None, K. *et al.* Evolution of placental invasion and cancer metastasis are causally
1047 linked. *Nature ecology & evolution* **3**, 1743–1753 (2019).

1048 55. Bulmer, J., Thrower, S. & Wells, M. Expression of epidermal growth factor receptor
1049 and transferrin receptor by human trophoblast populations. *American journal of*
1050 *reproductive immunology (New York, N.Y. : 1989)* **21**, 87–93 (1989).

1051 56. Wright JK *et al.* HER1 signaling mediates extravillous trophoblast differentiation in
1052 humans. *Biology of reproduction* **83**, 1036–1045 (2010).

57. Coorens, T. H. H. *et al.* Inherent mosaicism and extensive mutation of human placentas. *Nature 2021 592:7852* **592**, 80–85 (2021).

58. Angelo, M. *et al.* Multiplexed ion beam imaging of human breast tumors. *Nature Medicine* **20**, 436–442 (2014).

59. McCaffrey, E. F. *et al.* Multiplexed imaging of human tuberculosis granulomas uncovers immunoregulatory features conserved across tissue and blood. *bioRxiv* 2020.06.08.140426 (2020) doi:10.1101/2020.06.08.140426.

60. Risom, T. *et al.* Transition to invasive breast cancer is associated with progressive changes in the structure and composition of tumor stroma. *bioRxiv* 2021.01.05.425362 (2021) doi:10.1101/2021.01.05.425362.

61. Keren, L. *et al.* A Structured Tumor-Immune Microenvironment in Triple Negative Breast Cancer Revealed by Multiplexed Ion Beam Imaging. *Cell* **174**, 1373-1387.e19 (2018).

62. Howe, N. Better Skeletonization - File Exchange - MATLAB Central. https://www.mathworks.com/matlabcentral/fileexchange/11123-better-skeletonization.

63. D'Errico, J. distance2curve - File Exchange - MATLAB Central. https://www.mathworks.com/matlabcentral/fileexchange/34869-distance2curve.

Acknowledgements

We thank V. Winn, N. Vivanco, A. Moore, E. McCaffrey, D. Glass, T. Risom, J. P. Oliveria, K. O'Neill and C. Coutifaris for comments. M.A. is supported by 5U54CA20997105, 5DP5OD01982205, 1R01CA24063801A1, 5R01AG06827902, 5UH3CA24663303, 5R01CA22952904, 1U24CA22430901, 5R01AG05791504, and 5R01AG05628705 from NIH, W81XWH2110143 from DOD, and other funding from the Bill and Malinda Gates Foundation, Cancer Research Institute, the Parker Center for Cancer Immunotherapy, and the Breast Cancer Research Foundation. S.G is supported by the Bill and Melinda Gates Foundation OPP1113682. I.A. is an awardee of the

Weizmann Institute of Science – Israel National Postdoctoral Award Program for Advancing Women in Science. E.S is supported by National Science Scholarship, Agency for Science, Technology, and Research (A*STAR), Singapore.

Author contributions

S.G. assembled the tissue cohort, performed and designed experiments, annotated images, analyzed and interpreted data and wrote the manuscript. I.A. analyzed and interpreted data, wrote the manuscript. E.S. performed and designed experiments, annotated images, analyzed and interpreted data, wrote the manuscript. G.R. advised on cohort design, assembled tissue cohort, annotated images. A.B, N.G., G.M., M.S., W.G. and D.V.V. wrote software for image analysis. M.B. advised on experimental design and reagent validation. E.J. assembled cohort patient metadata. L.K. advised on computational analysis. Z.K. Prepared and validated reagents. S.K. Constructed the tissue microarray. S.W. annotated images. T.H. validated reagents and advised on experimental design. M.R. oversaw tissue microarray construction. M.A. conceived the study, advised on experimental design and data analysis, wrote the manuscript.

Supplementary table legends

Supplementary Table 1 - Patients table. This table provides patient meta-data such as age, ethnicity, body mass index, parity and relevant medical conditions such as HIV.

Supplementary Table 2 - Information on the histological characteristics of the blocks retrieved, including the presence of cell column anchoring villi. This table shows, for each patient's block, whether cell column anchoring villi were present (1) or absent (0), and the number of regions containing spiral arteries annotated as appropriate for TMA construction by the pathologist (Methods). In blocks containing ≥ 2 distinct, separate pieces of tissue, cell column villi were considered present if they were present on any piece containing pathologist annotations.

Supplementary Table 3 - Cell table. This table enumerates all single cells in this study and provides their location, morphological characteristics such as size and shape,

1109 marker expression, FlowSOM cluster assignment and cell type assignment.

1110 **Supplementary Table 4 - Positivity binary threshold for functional markers.**
1111 This table provides binary expression thresholds per functional marker- used to determine
1112 whether cells are positive for that marker (See methods).

1113 **Supplementary Table 5 - Artery properties and staging.** This table provides
1114 arteries meta-data, including their measured digitized morphological features (see
1115 Methods), manual stage and remodeling score δ.

1116 **Supplementary Table 6 - LDA coefficients for artery morphological features.**
1117 This table contains the coefficients per artery feature that define the LDA space used for
1118 digitized artery staging (Fig. 3n). For the features selected by the algorithm, their ld1 and
1119 ld2 coefficients are listed. Additional columns show the Z scored absolute values of these
1120 coefficients.

1121 **Supplementary Table 7 - Regression results for cell type proportions as a**
1122 **function of GA and δ.** This table provides the values plotted in Fig. 3o. Each row
1123 represents a cell proportion with those starting with R_ indication proportion out of all cells
1124 in the image, I_ - proportion out of immune cells in image, N_- proportion out of NK cells
1125 in image, M_ proportion out of macrophages in image, T_- proportion out of T cells in
1126 image, F_- proportion out of EVT in image, S_ proportion out of structural cells in image
1127 (Fig. 2b). The columns show values for the linear regression on per image proportions as
1128 function of GA and remodeling score δ: the log transformed ratio of R^2, the maximal
1129 obtained regression R^2 (maximal between GA and δ), the minimal obtained regression p-
1130 value and trend size (see Methods).

1131 **Supplementary Table 8 - Regression results for functional markers**
1132 **expression as a function of GA and δ.** This table provides the values plotted in Fig. 5a.
1133 Each row represents a combination of a cell type and a functional marker. The columns
1134 show values for the linear regression on per image marker positivity rates for the marker-
1135 cell type as function of GA and remodeling score δ: the log transformed ratio of R^2, the
1136 maximal obtained regression R^2 (maximal between GA and δ), the minimal obtained
1137 regression p-value and trend size (see Methods).

1138 **Supplementary Table 9 - Information on antibodies, metal reporters, staining**
1139 **concentrations, and parameters used for low-level processing of MIBI data.** This
1140 table contains, for each marker, relevant antibody information including clone, vendor,
1141 vendor ID, channel and elemental reporter, and final staining titers used. The parameters
1142 used for marker-specific low-level processing of MIBI data (background removal,
1143 denoising, and aggregate removal steps as previously described) are also shown.

1144 **Supplementary Table 10 - LD1 coefficients for markers expressed by EVT.**
1145 This table contains the coefficients per EVT expressed marker that define the LDA space
1146 used for measuring similarity between anatomical tissue compartments (see Methods,
1147 Extended Data Fig. 6c). For the markers selected by the algorithm, their ld1 coefficients
1148 are listed. An additional column shows the Z scored absolute values of these coefficients.

1149 **Supplementary Table 11 - LD1 values per EVT.** This table shows ld1 values per
1150 single EVT with LDA input- standardized marker expression values (see Methods,
1151 Extended Data Fig. 6c). Additional metadata such as EVT type, anatomical location, the
1152 image the cell was taken from is also provided.